Ocean Dynamics (2025) 75:25
https://doi.org/10.1007/s10236-025-01674-7

Direct numerical simulations of the nonbreaking surface-wave-induced turbulence

Haruka Imamura[1] · Yutaka Yoshikawa[1] · Yasushi Fujiwara[2]

Received: 25 October 2024 / Accepted: 25 February 2025

Abstract

Direct numerical simulations of the turbulence induced by nonbreaking surface waves were conducted to clarify the turbulence generation mechanism and evaluate the turbulent mixing intensity with a sigma-coordinate free-surface nonhydrostatic model. One of the simulations was modeled after a previously reported laboratory experiment with a wave of 30 cm wavelength and 1 cm amplitude freely propagating on the initially stratified water under a windless condition. The simulation showed that organized vortex pairs like Langmuir circulations (LCs) grew, and the water was mixed vertically. The enstrophy budget analysis revealed that the vortex pairs were generated nonlocally through the interaction between surface waves and a surface shear flow, the same mechanism for the LCs, except that the flow is forced by not the wind but the virtual wave stress due to viscous wave attenuation. The analysis also revealed that the local turbulence generation mechanism by the wave orbital motions (as inferred by the previous laboratory study) did not work in our simulated turbulence. The simulated eddy diffusivity was $\boldsymbol{O}(10^{-5}\ \mathrm{m}^2\ \mathrm{s}^{-1})$ and its vertical profile and temporal changes were different from those of the parameterized diffusivity based on the local turbulence generation mechanism. The nonbreaking wave-induced mixing observed in our simulations under windless conditions is expected to occur in the real open ocean. These results suggest that to parameterize this mixing, parameterization of the nonlocal Langmuir turbulence, with wind stress replaced by virtual wave stress, could be an effective approach.

Keywords Surface wave · Wave-resolving simulation · Turbulence · Ocean surface mixing

1 Introduction

An increasing number of studies have focused on ocean surface turbulent mixing induced by the wave orbital motions of nonbreaking surface waves (e.g., D'Asaro 2014). Langmuir circulations (LCs), which are vortex pairs generated by the interaction between surface waves and wind-induced shear flow, are one well-known example of processes that induce such mixing. The mechanism of this wave-current interaction is explained by the Craik and Leibovich (CL) theory (e.g., Craik and Leibovich 1976). A linear stability analysis of the wave-averaged momentum equation with the wave-current interaction term (CL equation) shows that the streamwise vortex grows exponentially when the wave propagates in the downwind direction (Leibovich 1983). The turbulence generated by LCs can penetrate to a depth greater than the e-folding depth of the wave orbital velocity (Grant and Belcher 2009). This indicates that the turbulence is generated nonlocally rather than locally by the wave. The mechanism of this turbulence is referred to as the CL2 mechanism in this paper.

Recent laboratory experiments (Babanin and Haus 2009; Dai et al. 2010; Savelyev et al. 2012; Bogucki et al. 2020) suggest on the other hand that surface turbulent mixing is also induced only by nonbreaking surface waves, i.e., wind is not necessary for the wave-induced turbulent mixing. Specifically, Dai et al. (2010) conducted the wave tank experiments

Responsible Editor: Yu-Lin Chang

✉ Haruka Imamura
imamurahrk@kugi.kyoto-u.ac.jp

Yutaka Yoshikawa
yosikawa@kugi.kyoto-u.ac.jp

Yasushi Fujiwara
fujiwara@port.kobe-u.ac.jp

1 Graduate School of Science, Kyoto University, Kitashirakawa-Oiwake, Sakyo, Kyoto 6068502, Japan

2 Graduate School of Maritime Sciences, Kobe University, Fukae Minami-machi 5-1-1, Higashinada-ku, Kobe, Hyogo 6580022, Japan

Published online: 07 March 2025

under windless condition with waves propagating on initially stratified water for several tens of minutes, and demonstrated that stratified water was vertically mixed by the wave. This paper is concerned with this nonbreaking surface-wave-induced mixing under windless condition, which is hereafter referred to as windless (WL) wave-induced mixing.

Qiao et al. (2004) first paid attention to the WL wave-induced mixing and assumed that wave orbital motion itself interacts *locally* with turbulence at each depth, which we hereafter refer to as the local interaction (LI) mechanism. The turbulence generation through the LI mechanism is parameterized originally in Qiao et al. (2004) with the eddy diffusivity B_υ, based on Prandtl's mixing length theory, where the mixing length and the shear are taken respectively as the wave particle displacement and the vertical shear of the wave orbital velocity. Later, Qiao et al. (2016) took into account the interaction between the Stokes drift and turbulence and then updated the parameterization, though the modified one has the same mathematical form as the original B_υ. For a monochromatic linear wave, B_υ becomes (Dai et al. 2010)

$$B_\upsilon = \alpha a^3 k\omega \left[\frac{\sinh k(z+h)}{\sinh kh}\right]^3, \qquad (1)$$

where a, k, and ω are the wave amplitude, wavenumber, and angular frequency, respectively, and z and h is the vertical coordinate and average water depth, respectively. Dai et al. (2010) reported that observed destratification in their experiments was explained by B_υ with a coefficient $\alpha = 1$. The parameterizations based on the LI mechanism were also developed by other studies (Hu and Wang 2010; Pleskachevsky et al. 2011) and showed some improvements in simulating the upper ocean structure (e.g., Wu et al. 2015, Chen et al. 2018, Wang et al. 2019).

Although the LI mechanism appears to be consistent with the observations in the laboratory experiment and is supported by the improvements in the model performance, "the validity of these arguments has come under serious scrutiny in the literature" (D'Asaro 2014). It should be noted that conditions under which the LI mechanism occurs remain unclear. Babanin (2006) proposed a threshold wave-amplitude-based Reynolds number $a^2\omega/\nu = 3000$ for the onset of the LI mechanism, where ν is the kinematic viscosity of the water. This threshold was supported by laboratory experiments conducted by Babanin and Haus (2009). In contrast, Beyá et al. (2012) reported that no evidence of turbulent mixing was observed up to $a^2\omega/\nu = 7000$ in their wave tank experiments. Additionally, Li et al. (2019) pointed out that the relationship between turbulence generated by CL2 and LI mechanism remains unclear. These uncertainties stem from the lack of direct experimental validation of the LI mechanism, particularly with respect to the numerical simulation that allow for the detailed dynamical analysis.

Recent numerical experiments with wave-resolving models provided on the other hand that CL2 mechanism is another possible mechanism of the WL wave-induced mixing. The numerical experiments showed counter-rotating streamwise vortex pairs like LCs in the presence of nonbreaking surface waves propagating over unstratified water under windless conditions (Tsai et al. 2015, 2017; Fujiwara et al. 2020). Tsai et al. (2017) showed good agreements between the spanwise wavenumbers of the simulated vortex pairs and the unstable wavenumbers expected from the linear stability analysis of the CL equation with the shear flow generated by virtual wave stress (VWS) (Longuet-Higgins 1953). Fujiwara et al. (2020) simulated an averaged flow field with the CL equation imposing the VWS at the surface and confirmed that the observed vortex pairs are similar to those simulated in the corresponding wave-resolving simulation of the attenuating surface wave. These results demonstrate that the interaction between surface waves and VWS-induced shear flow via the CL2 mechanism generates vortex pairs and corresponding streamwise streaks, as observed in the laboratory experiments of Savelyev et al. (2012).

These numerical simulations experimentally validate that the CL2 mechanism works during the initial growing stage of streamwise vortex pairs/streaks under the windless conditions. However, in a fully turbulent stage of the WL wave-induced mixing, it remains unclear whether the CL2 mechanism continues to work or whether the LI mechanism works simultaneously or predominantly. It is because Tsai et al. (2017) stopped the simulation immediately after the amplitudes of the vortex pairs became finite while Fujiwara et al. (2020) used lower Reynolds number than the laboratory experiments and hence the simulated turbulence was weak. Identification of the dominant mechanism leads to better parameterization of the mixing. For example, if the CL2 mechanism is the unique mechanism, the effects of WL wave-induced mixing can be evaluated using the same parameterization scheme as LCs with wind stress replaced by VWS. If both the LI and CL2 mechanisms work, two effects should be evaluated separately.

The purpose of this study is to clarify the turbulent generation mechanism that induces the WL wave-induced mixing and to evaluate the mixing intensity. To this end, we run a direct numerical simulation (DNS) using a similar experimental design to the laboratory experiment of Dai et al. (2010) in which the LI mechanism was suggested to work, though our DNSs exclude non-essential factors in the proposed LI mechanism (e.g., side walls in the laboratory experiment). Additional simulations are conducted to test the sensitivities of the results on water stratification, wave parameters, and computational domain. The structure of the paper is as follows. Section 2 describes the numerical model used in this study, and Section 3 outlines our DNS setup. The results of the DNS are presented in Section 4, where the turbulence generation mechanism and the mixing intensity are analyzed. The sensitivities tests are shown in Section 5. Finally, concluding remarks are presented in Section 6.

2 Numerical model

The numerical model used in this study is a sigma-coordinate free-surface nonhydrostatic model, similar to the models of Tsai and Hung (2007), Yang and Shen (2011), and Fujiwara et al. (2020).

2.1 Governing equations and boundary conditions

We consider a three-dimensional rectangular domain bounded by a rigid bottom at $z = -h$ and a free surface at $z = \eta(x, y, t)$ with periodic boundary conditions in the horizontal directions, where x, y, and z represent the Cartesian coordinates with z pointing upward and t as the time. The still water depth h is set to be constant and the water surface elevation $\eta(x, y, t)$ is assumed to be a single-value function with its mean vertical position at $z = 0$. System rotation is not considered owing to the short timescale of our experiment.

The water used in this study is an incompressible Boussinesq fluid. Its density ρ is assumed to depend linearly on water temperature; hence, buoyancy b, instead of temperature, is considered in this study. The governing equations are the momentum equations, continuity equation, advection-diffusion equation of buoyancy, and conservation equation of water volume:

$$\frac{\partial u}{\partial t} + u\frac{\partial u}{\partial x} + \upsilon\frac{\partial u}{\partial y} + w\frac{\partial u}{\partial z} = -g\frac{\partial \eta}{\partial x} - \frac{1}{\rho_0}\frac{\partial p}{\partial x} + \frac{\partial T^{xx}}{\partial x} + \frac{\partial T^{yx}}{\partial y} + \frac{\partial T^{zx}}{\partial z}, \tag{2a}$$

$$\frac{\partial \upsilon}{\partial t} + u\frac{\partial \upsilon}{\partial x} + \upsilon\frac{\partial \upsilon}{\partial y} + w\frac{\partial \upsilon}{\partial z} = -g\frac{\partial \eta}{\partial y} - \frac{1}{\rho_0}\frac{\partial p}{\partial y} + \frac{\partial T^{xy}}{\partial x} + \frac{\partial T^{yy}}{\partial y} + \frac{\partial T^{zy}}{\partial z}, \tag{2b}$$

$$\frac{\partial w}{\partial t} + u\frac{\partial w}{\partial x} + \upsilon\frac{\partial w}{\partial y} + w\frac{\partial w}{\partial z} = -\frac{1}{\rho_0}\frac{\partial p}{\partial z} + b + \frac{\partial T^{xz}}{\partial x} + \frac{\partial T^{yz}}{\partial y} + \frac{\partial T^{zz}}{\partial z}, \tag{2c}$$

$$\frac{\partial u}{\partial x} + \frac{\partial \upsilon}{\partial y} + \frac{\partial w}{\partial z} = 0, \tag{2d}$$

$$\frac{\partial b}{\partial t} + u\frac{\partial b}{\partial x} + \upsilon\frac{\partial b}{\partial y} + w\frac{\partial b}{\partial z} = \kappa\left(\frac{\partial^2 b}{\partial x^2} + \frac{\partial^2 b}{\partial y^2} + \frac{\partial^2 b}{\partial z^2}\right) \tag{2e}$$

$$\frac{\partial \eta}{\partial t} + \frac{\partial}{\partial x}\int_{-h}^{\eta} u\,dz + \frac{\partial}{\partial y}\int_{-h}^{\eta} \upsilon\,dz = 0. \tag{2f}$$

Here, u, υ, and w are respectively the x-, y-, and z-components of velocity; ρ_0 is the reference density; g is the gravitational acceleration; and p is an internal component of total pressure ϕ given by

$$\phi = \rho_0 g(\eta - z) + p, \tag{3}$$

where the atmospheric pressure is assumed to be constant and is omitted without loss of generality. The viscous stress tensor components T^{ij} are defined as

$$T^{ij} = \nu\left(\frac{\partial u_i}{\partial x_j} + \frac{\partial u_j}{\partial x_i}\right), \tag{4}$$

where $i, j = 1, 2, 3$, $(x_1, x_2, x_3) = (x, y, z)$, and $(u_1, u_2, u_3) = (u, \upsilon, w)$. The kinematic molecular viscosity ν and molecular diffusivity κ are assumed to be constant.

The rigid bottom boundary (at $z = -h$) is assumed to be free-slip and insulated:

$$\frac{\partial u}{\partial z} = 0, \tag{5a}$$

$$\frac{\partial \upsilon}{\partial z} = 0, \tag{5b}$$

$$w = 0, \tag{5c}$$

$$\frac{\partial p}{\partial z} = \rho_0 b, \tag{5d}$$

$$\frac{\partial b}{\partial z} = 0. \tag{5e}$$

The boundary condition of the internal component of the total pressure [Eq. 5d] is derived using Eq. 2c.

At the surface boundary (at $z = \eta$), the velocity and pressure boundary conditions are set from the dynamical boundary conditions (e.g., Tsai and Hung 2007). Without wind stress, the surface boundary conditions are as follows:

$$\frac{\partial u}{\partial z} = \frac{1}{\eta_x^2 + \eta_y^2 - 1}\left\{-\eta_y(1 + \eta_x^2 - \eta_y^2)\left(\frac{\partial \upsilon}{\partial x} + \frac{\partial u}{\partial y}\right) - 2\eta_x(1 + \eta_y^2)\frac{\partial \upsilon}{\partial y} - (\eta_x^2 + \eta_y^2 - 1)\frac{\partial w}{\partial x} - 2\eta_x(2 - \eta_y^2)\frac{\partial u}{\partial x}\right\}, \tag{6a}$$

$$\frac{\partial \upsilon}{\partial z} = \frac{1}{\eta_x^2 + \eta_y^2 - 1}\left\{-\eta_x(1 - \eta_x^2 + \eta_y^2)\left(\frac{\partial \upsilon}{\partial x} + \frac{\partial u}{\partial y}\right) - 2\eta_y(1 + \eta_x^2)\frac{\partial u}{\partial x} - (\eta_x^2 + \eta_y^2 - 1)\frac{\partial w}{\partial y} - 2\eta_y(2 - \eta_x^2)\frac{\partial \upsilon}{\partial y}\right\}, \tag{6b}$$

$$\frac{\partial w}{\partial z} = -\frac{\partial u}{\partial x} - \frac{\partial \upsilon}{\partial y}, \tag{6c}$$

$$p = \sigma\kappa_c + \frac{2\rho\nu}{1 + \eta_x^2 + \eta_y^2}$$

$$\left\{\eta_x^2 \frac{\partial u}{\partial x} + \eta_y^2 \frac{\partial \upsilon}{\partial y} + \frac{\partial w}{\partial z} + \eta_x \eta_y \left(\frac{\partial \upsilon}{\partial x} + \frac{\partial u}{\partial y}\right) - \eta_x \left(\frac{\partial w}{\partial x} + \frac{\partial u}{\partial z}\right) - \eta_y \left(\frac{\partial \upsilon}{\partial z} + \frac{\partial w}{\partial y}\right)\right\}, \tag{6d}$$

where $\eta_x = \partial\eta/\partial x$ and $\eta_y = \partial\eta/\partial y$. The surface tension is denoted by σ and $\kappa_c = \nabla \cdot \hat{\mathbf{n}}$ is the surface curvature, where $\hat{\mathbf{n}}$ is the unit vector normal to the surface. The surface is assumed to be insulated against buoyancy (heat). As the surface slope is expected to have a negligible impact on the buoyancy flux in our experiment, the insulation condition at the free surface is approximated as that at the flat surface:

$$\frac{\partial b}{\partial z} = 0. \tag{6e}$$

The governing equations and boundary conditions are transformed from the Cartesian coordinates, (x, y, z, t), to the sigma coordinates, (x^*, y^*, z^*, t^*) where $x^* = x$, $y^* = y$, $z^* = (z + h)/(h + \eta)$, and $t^* = t$, as in Tsai and Hung (2007). The sigma coordinates enable the simulation of flows with a high vertical resolution near the surface.

2.2 Computational method

The governing equations and boundary conditions are discretized as follows. In the horizontal direction, a pseudo-spectral method based on the Fourier series is used. To reduce the numerical error, zero-filling of the spectral coefficients above two-thirds of the Nyquist wavenumber is applied (e.g., Tsai and Hung 2007, Fujiwara et al. 2020). A second-order finite-difference method with a staggered grid is used in the vertical direction. The horizontal velocities u and υ, pressure p, and buoyancy b are arranged at the cell center, whereas the vertical velocity w is arranged at the cell interface. For the viscous stress tensor T^{xx}, T^{xy}, T^{yy}, and T^{zz} are arranged at the cell center, whereas T^{xz} and T^{yz} are arranged at the cell interface. For temporal integration, the fourth-order Runge-Kutta scheme is adopted.

The internal component of the total pressure p is obtained by solving the Poisson equation derived from the momentum and continuity equations. In this derivation, we adopt the same strategy as in Fujiwara et al. (2020). The pressure equation is solved using the fixed-point iteration scheme described in Tsai and Hung (2007) and Fujiwara et al. (2020). The iteration continues until the maximum pressure change from the previous iteration becomes 10^{-8} times smaller than the maximum pressure.

3 Model setup

We conducted a direct numerical simulation (DNS) of a surface gravity wave with a wavelength (λ) of 30 cm and an initial amplitude (a) of 1 cm propagating on water with an average depth (h) of 20 cm with reference to the laboratory experiment with $\lambda = 30$ cm in Dai et al. (2010). Physical parameter values were chosen as $g = 9.8$ m s^{-2}, $\rho_0 = 1.0 \times 10^3$ kg m^{-3}, $\nu = 1.0 \times 10^{-6}$ m^2 s^{-1}, $\kappa = 1.4 \times 10^{-7}$ m^2 s^{-1}, and $\sigma = 7.2 \times 10^{-2}$ kg s^{-2}. The physical parameters here may not be exactly the same as those in Dai et al. (2010), but the differences are tiny and do not change our conclusions. The computational domain was set as $0 \leq x \leq \lambda$, $0 \leq y \leq \lambda$, and $-h \leq z \leq \eta$ and was discretized by 256, 256, and 256 grid points.

A third-order Stokes wave with $\lambda = 30$ cm and $a = 1$ cm propagating in the positive x-direction was used as the initial condition for velocities u and w and surface elevation η. The initial value for velocity υ is zero everywhere. The corresponding initial wave steepness ak was 0.21 and the wave period T_w was 0.43 s. The initial buoyancy stratification ($\partial_z b$) was set as 5.5×10^{-2} s^{-2} for the corresponding water-temperature stratification (5 °C/8 cm), which was similar to that in Dai et al. (2010). The initial random perturbations were added to the velocity acceleration terms in the x-, y-, and z-components, whose amplitudes were 4% of the maximum acceleration of the initial Stokes wave and decayed with depth with $\sinh kz$ for u and $\cosh kz$ for υ and w. Magnitude of the initial kinetic energy does not qualitatively change results described later (not shown). The simulation was conducted for 600 T_w with a time-step interval of $\Delta t = T_w/200$.

Note that the there are some differences in experimental settings between the laboratory experiment by Dai et al. (2010) and our DNS. Major differences are domain size and boundary condition; In the laboratory experiment, a tank of 5 m length and 0.3 m width was used with a wave generator and a wave absorber at the x-boundary and side walls at the y-boundary with some heat flux through boundaries, while in our DNS, a smaller (0.3 m long, 0.3 m wide) domain is used with periodic boundary conditions at both x- and y- boundaries with no heat flux through the boundaries. We assume that these differences have no impact on the LI mechanism where the wave orbital motion itself interacts locally with turbulence at each depth.

To visualize the water motion, we simulated a passive tracer field. The tracer concentration (denoted as d) follows the same governing equation as the buoyancy [Eq. 2e]. There is no tracer flux at the bottom ($\partial_z d = 0$), whereas the tracer value is always set to unity ($d = 1$) at the surface. Initially, d was set to zero, except at the surface. The model performance was examined against the momentum conservation, dispersion relation of the 3rd order Stokes wave, and wave amplitude viscous attenuation, all of which show good agreements with what are expected theoretically (not shown). The present vertical grid spacing is unable to fully resolve the viscous boundary layer, but it is sufficient to reproduce the VWS induced shear flow (Fujiwara et al. 2020). The buoyancy boundary layer is also unresolved, but simulated buoyancy profile is reasonable as the VWS flow profile is. In the following, the x- and y-direction are sometimes referred to as streamwise and spanwise direction, respectively.

4 Results

4.1 Simulated fields

Figures 1a-d show the near-surface ($z^* = 0.998$, where $z^* = 0$ and $z^* = 1$ correspond respectively to the bottom and the surface) distributions of the simulated velocity and passive-tracer concentration at $t = 70\ T_w$. The spatial patterns of the x-component u (Fig. 1a) and the z-component w (Fig. 1c) of velocity illustrate that the wave orbital motion

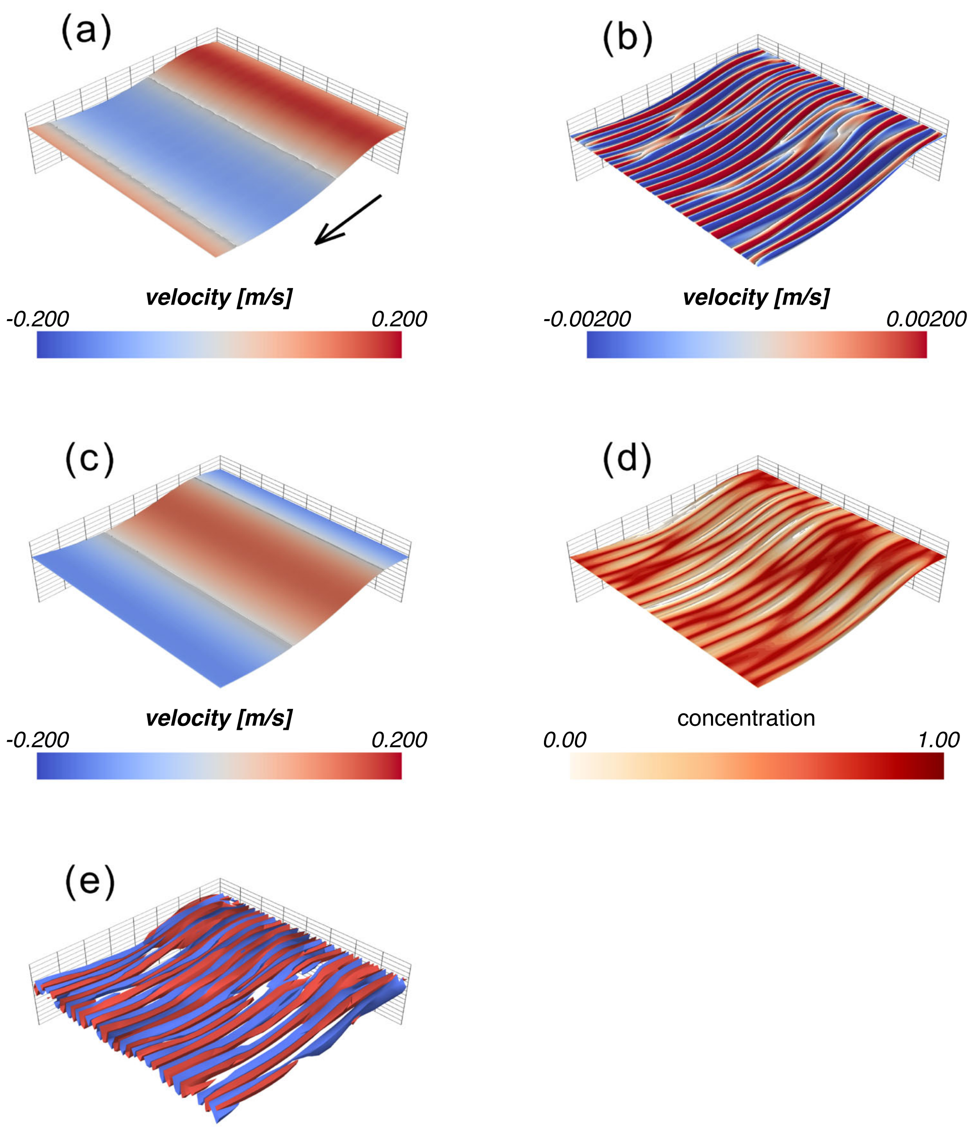

Fig. 1 Near-surface (z^*=0.998) distributions of the velocities (a) u, (b) v, and (c) w and (d) passive tracer concentration d, and (e) isosurface distributions of the streamwise vorticity at $t = 70\ T_w$. In Panel e, the red/blue color represents positive/negative vorticity with an absolute value of 0.08 [1/s]. The wave propagates in the direction of the black arrow shown in Panel a

velocity dominates the simulated u and w fields. In contrast, the y-component υ (Fig. 1b) of the velocity and passive tracer concentration d (Fig. 1d) fields show streaks elongated almost uniformly in the wave propagation direction as observed in the previous laboratory (Savelyev et al. 2012) and numerical (Tsai et al. 2015, 2017) experiment, suggesting the presence of motion other than the wave orbital motion. Figure 1e illustrates the isosurfaces of the streamwise vorticity, which elongate in the wave propagation direction. Positive and negative vorticities alternate in the spanwise direction, indicating the presence of the organized vortex pairs like LCs.

To investigate the simulated velocity fields in detail, the squared coherence and the phase difference are examined on the horizontal wavenumber space (k_x, k_y), where k_x and k_y is respectively the x- and y-directional wavenumber normalized by the wavelength of the Stokes wave (λ) imposed as the initial condition. In the presence of surface waves propagating in the x- (y-) direction, the high coherence and $\pm\pi/2$ phase difference between u and w (υ and w), which is the polarization relation of the surface wave, are expected. If the organized vortex pairs like LCs elongate in the x-direction, the velocity field exhibits the following characteristics: downwelling (negative w) along the lines of the high streamwise velocity (positive u), toward which the spanwise velocity (υ) converges near the surface. These velocity fields are expected to show the high coherence between u and w and between υ and w, and the phase difference of $\pm\pi$ between u and w and $-\pi/2$ between υ and w in the small k_x wave number region.

Figures 2 and 3 display the squared coherence and the phase difference between u and w and between υ and w as well as the kinetic energy [KE, $(u^2 + \upsilon^2 + w^2)/2$] on the horizontal wavenumber space (k_x, k_y) at $t = 70\ T_w$ (Fig. 2) and $t = 560\ T_w$ (Fig. 3). Here the power spectrum and cross spectrum used in calculating the squared coherence and phase difference are calculated at every $T_w/10$ and then averaged over T_w. Specifically, Figs. 2 and 3 use the velocity fields of $69.5\ T_w \leq t < 70.5\ T_w$ and $559.5\ T_w \leq t < 560.5\ T_w$, respectively. Firstly, both at $t = 70\ T_w$ (Fig. 2) and $560\ T_w$ (Fig. 3), the third-order Stokes wave imposed as the initial condition is evident in the coherence and phase difference at (k_x, k_y)=(1,0), (2,0), and (3,0) where kinetic energy is large ($> 10^{-3}$ m^2 s^{-2}). Hereafter this wave is referred to as the primary wave. On the other hand, it is also confirmed that other wave numbers than those of the primary wave show high coherence and the phase relations (the polarization relations) of the surface waves propagating in the x- or y-direction such as $(k_x, k_y) = (3, 2)$ at $t = 70\ T_w$ (Fig. 2) and $(k_x, k_y) =$ (0, 1), (2, 3), (3, 2), and (4, 2) at $t = 560\ T_w$ (Fig. 3), with their maximum kinetic energy being less than 10^{-8} m^2 s^{-2} at t=70 T_w and 10^{-6} m^2 s^{-2} at $t = 560\ T_w$. These waves are hereafter called as secondary waves. The absence of the

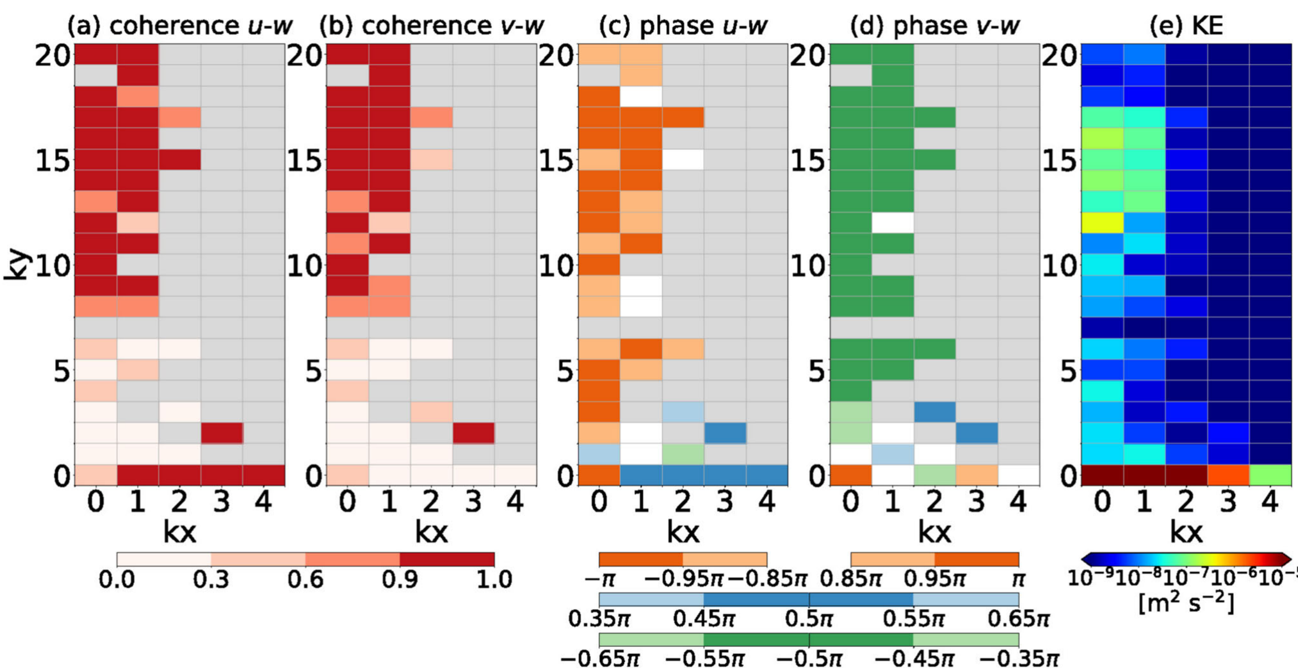

Fig. 2 Distributions of near-surface squared coherence (a and b), phase (c and d), and kinetic energy (KE, e) over the horizontal wavenumber space (k_x, k_y) at $t = 70\ T_w$. Coherence and phase are shown in the wavenumbers with KE being more than 2.3×10^{-9} m^2 s^{-2}. The lower left color bar is for Panels a and b, the lower center three color bars are for Panels c and d, and the lower right color bar is for Panel e. Gray boxes in Panels a-d represent the KE values under the criteria. White boxes in Panels c and d indicate phase outside of the color bar ranges

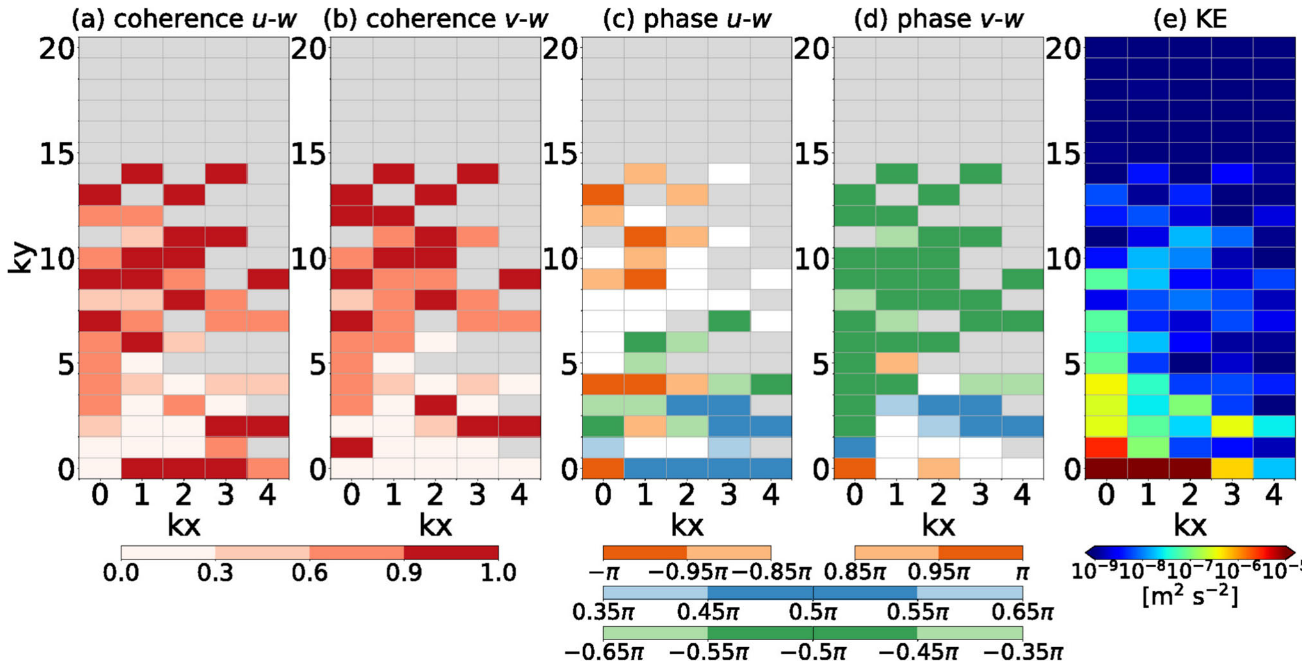

Fig. 3 Same as Fig. 2, but at $t = 560\ T_w$

secondary waves in an experiment without an initial perturbation (not shown) suggests that non-wave-orbital motions, such as vortex pairs we describe in the following, excites these secondary waves. Lastly, the coherence and phase relations corresponding to the vortex pairs are found around $0 \le k_x \le 1$, $9 \le k_y \le 17$ at $t = 70\ T_w$ (Fig. 2) and $0 \le k_x \le 2$, $9 \le k_y \le 14$ at $t = 560\ T_w$ (Fig. 3), whose maximum kinetic energy is 10^{-7} m^2 s^{-2} at $t = 70\ T_w$ and 10^{-8} m^2 s^{-2} at $t = 560\ T_w$. The wavenumbers of the vortex pairs at $t = 70\ T_w$ are consistent with those of υ and tracer streaks shown in Figs. 1b and d, indicating that the streaks correspond to the vortex pairs. These spectral analysis reveal that the dominant features of the simulated velocity field are primary wave, secondary waves, and vortex pairs.

In order to decompose surface (both primary and secondary) waves component and perturbation component (including vortex pairs), the surfaces waves (SWs) and perturbation component of velocity are defined on the basis of the horizontal wavenumber distribution of the spectra: waves component $\tilde{(\cdot)}$ and perturbation component $(\cdot)'$ defined as

$$\text{waves} \quad 0 \le k_x \le 1,\ 0 \le k_y \le 2 \quad \text{and} \quad k_x \ge 2,\ 0 \le k_y \le 3, \tag{7}$$

$$\text{perturbation} \quad 0 \le k_x \le 1,\ k_y \ge 3 \quad \text{and} \quad k_x \ge 2,\ k_y \ge 4. \tag{8}$$

The near-surface distributions of the perturbation velocity and tracer at $t = 70\ T_w$ and $560\ T_w$ are shown in Fig. 4. The streaky structures are evident in the perturbation velocity as well as tracer field at $t = 70\ T_w$ and $560\ T_w$. The streaks get undulating and their spanwise intervals get wider with time, which is consistent with that k_x and k_y corresponding to the vortex pairs increase and decrease respectively as shown in Figs. 2 and 3. We note that no streaks were observed in the experiment without an initial perturbation (not shown), indicating that the background vorticity is amplified by the surface waves.

The temporal evolutions of the surface-integrated perturbation kinetic energy, $E_{k'} = (u'^2 + \upsilon'^2 + w'^2)/2$, and each velocity variance $E_{u'} = u'^2/2$, $E_{\upsilon'} = \upsilon'^2/2$, and $E_{w'} = w'^2/2$ are shown in Fig. 5a. The temporal evolutions of its growth rate, $\beta = d(\log E)/d(t/T_w)$, are shown in Fig. 5b. The surface-integrated perturbation kinetic energy grows almost exponentially until $t \simeq 80\ T_w$ (hereafter referred as growing stage) and then decreases slowly until the end of the simulation (hereafter referred as mature stage). In the growing stage, the anisotropy of velocity variances and temporal changes of growth rates are consistent with the results of Tsai et al. (2015).

Figure 6 shows the tracer (Figs. 6a,c) and buoyancy (Figs. 6b,d) distributions in the y-z plane at $x = 0.5\ \lambda$ at $t = 70\ T_w$ (near the end of the growing stage, top row) and at $t = 560\ T_w$ (the mature stage, bottom row). The water with a high tracer concentration penetrate to greater depths with

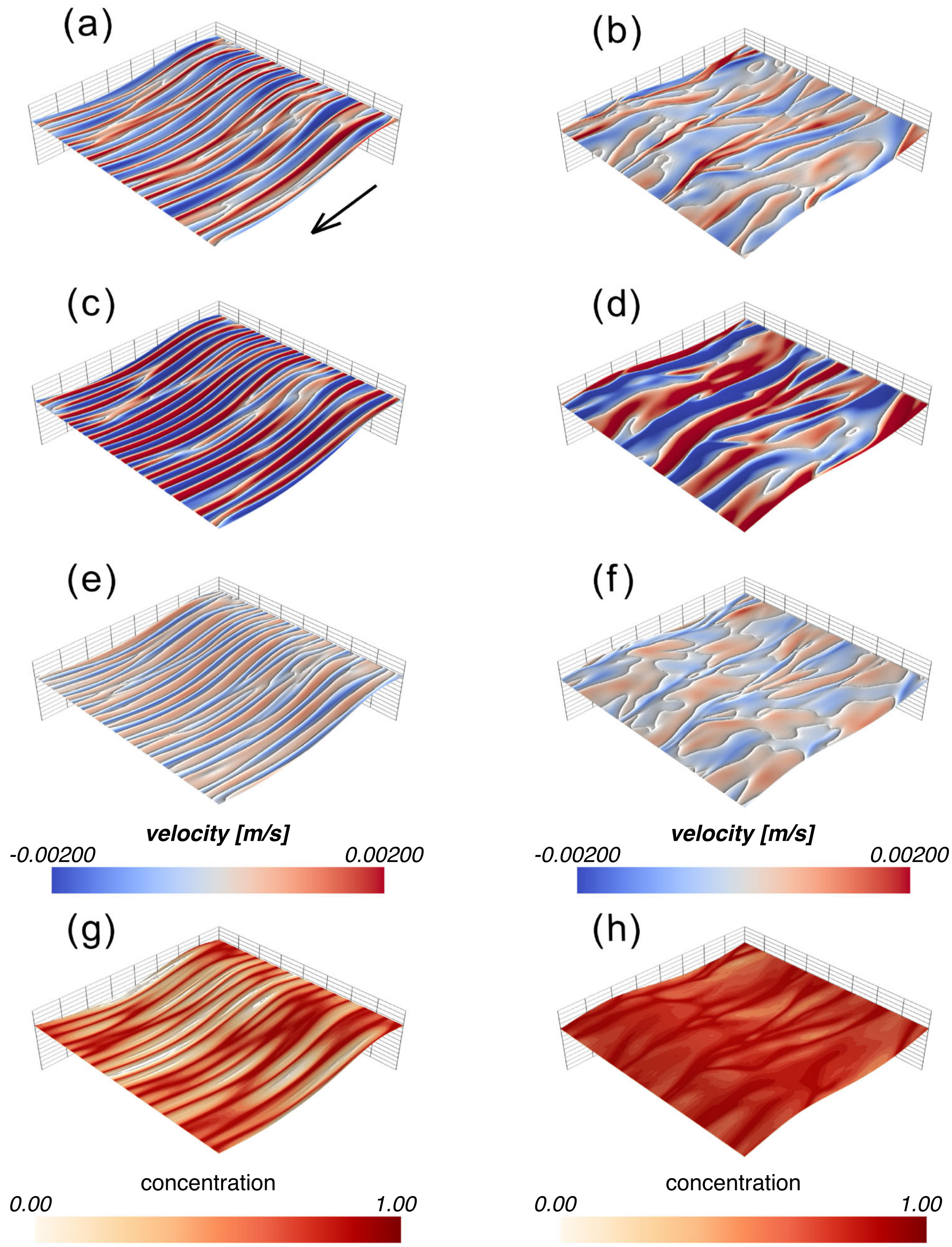

Fig. 4 Near-surface (z^*=0.998) distributions of the perturbation component velocities, defined as Eqs. 7 and 8, u'(a and b), v' (c and d), and w'(e and f), and the tracer concentration d (g and h) at $t = 70\ T_w$ (left panels) and $t = 560\ T_w$ (right panels). The primary wave propagates in the direction of the black arrow shown in Panel a. Panel g is the same as Fig. 1d

time in the form of plumes or thermals (Figs. 6a,c), which represent part of the vortex pairs as expected from the good correspondence between the tracer and perturbation velocity fields (e.g., Fig. 4). Initially stratified water is clearly destratified from near the surface with time (Figs. 6b,d), as observed in Dai et al. (2010). These simulated results demonstrate that nonbreaking surface waves under windless condition generate vortex pairs that deepen with time and induce turbulent mixing.

4.2 Enstrophy budget

In this subsection, the mechanism of the WL wave-induced mixing observed in Section 4.1 is examined. A typical approach is the turbulent kinetic energy budget analysis. In fact, Tsai et al. (2015) conducted such an analysis with phase-resolved averages in the wave-following (z^*) coordinate. However, in this study, we choose to analyze enstrophy (squared vorticity) budgets in the Eulerian coordinate (z coor-

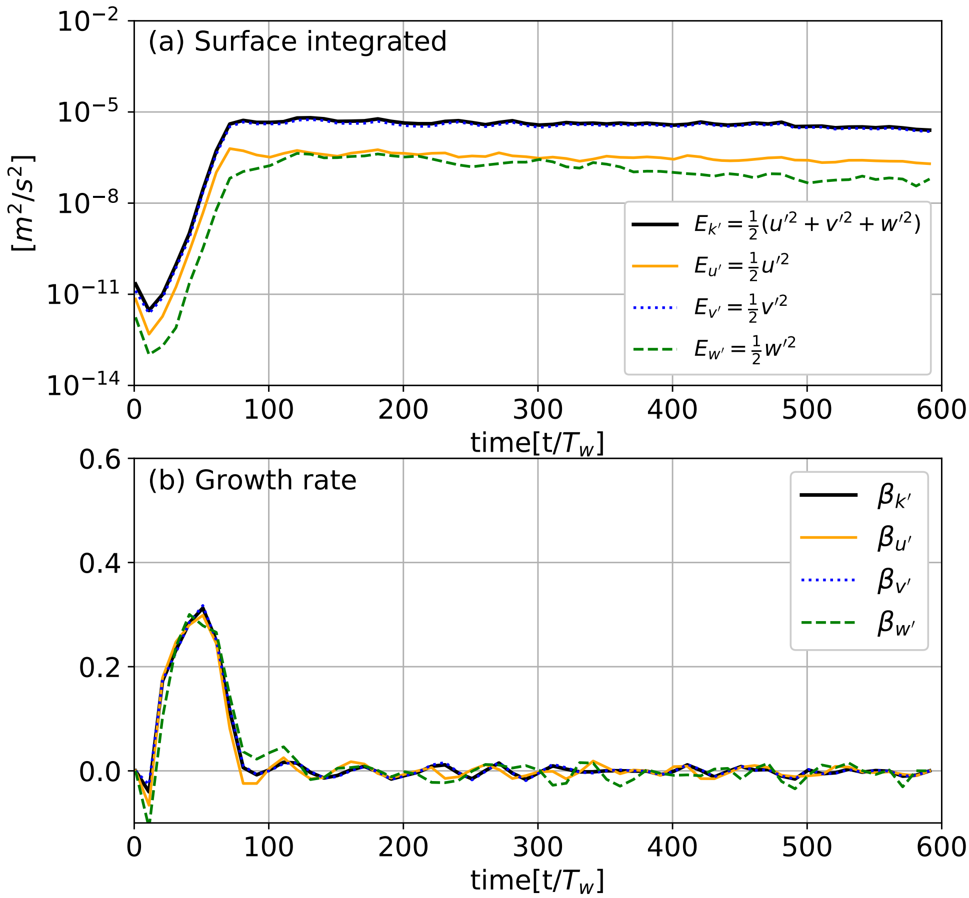

Fig. 5 Temporal evolutions of the surface-integrated (a) perturbation kinetic energy $E_{k'}$ and each velocity variance $E_{u'}$, $E_{\upsilon'}$, and $E_{w'}$ and (b) corresponding growth rate $\beta_{k'}$, $\beta_{u'}$, $\beta_{\upsilon'}$, and $\beta_{w'}$. The horizontal axis shows time normalized by the wave period of the primary wave

dinate). One reason for this choice is to completely separate the rotational turbulent motions out of irrotational surface waves, though the separation by Eqs. 7 and 8 is fairy successful. The other reason is that the analysis in the wave-following coordinate as made in Tsai et al. (2015) makes the Eulerian mean current and the Stokes drift current unseparatable, preventing comprehensive understanding of the interaction between current and waves (e.g., Fujiwara et al. 2020). The all simulated data were linearly interpolated from z^* to z coordinate before analyzing the enstrophy in the Eulerian coordinate, and the analysis was performed below the minimum water level ($-h \leq z \leq -a$). Figure 7 displays the temporal evolutions of the vertical profiles of the xy-averaged enstrophy $\overline{|\boldsymbol{\zeta}|^2}^{xy}/2$ and tracer concentration $\overline{d}^{xy}$. Here, $\boldsymbol{\zeta} = (\zeta_x, \zeta_y, \zeta_z) = \nabla \times \mathbf{v}$ is the vorticity vector where $\mathbf{v} = (u, \upsilon, w)$ represents the velocity vector; and $\overline{(\cdot)}^{xy}$ represents the horizontal average along the constant z. Good correspondence between the regions of the high enstrophy and the high tracer concentration throughout the experiment shows that the enstrophy budget analysis is a reasonable approach to reveal the mixing mechanism.

By multiplying vorticity component (ζ_i) with the corresponding vorticity equation [$\partial_t \zeta_i$, obtained from Eqs. 2a-2c], the following equations for $\zeta_i^2/2$ are obtained:

$$\partial_t \frac{\zeta_x^2}{2} = \underbrace{\zeta_x[\nabla \times (\tilde{\mathbf{v}} \times \boldsymbol{\zeta})]_x}_{(a)} + \underbrace{\zeta_x[\nabla \times (\mathbf{v}' \times \boldsymbol{\zeta})]_x}_{(b)} + \underbrace{\zeta_x \partial_y b}_{(c)} + \underbrace{\zeta_x[\nu \nabla^2 \boldsymbol{\zeta}]_x}_{(d)}, \tag{9a}$$

$$\partial_t \frac{\zeta_y^2}{2} = \underbrace{\zeta_y[\nabla \times (\tilde{\mathbf{v}} \times \boldsymbol{\zeta})]_y}_{(a)} + \underbrace{\zeta_y[\nabla \times (\mathbf{v}' \times \boldsymbol{\zeta})]_y}_{(b)} + \underbrace{(-\zeta_y \partial_x b)}_{(c)} + \underbrace{\zeta_y[\nu \nabla^2 \boldsymbol{\zeta}]_y}_{(d)}, \tag{9b}$$

$$\partial_t \frac{\zeta_z^2}{2} = \underbrace{\zeta_z[\nabla \times (\tilde{\mathbf{v}} \times \boldsymbol{\zeta})]_z}_{(a)\ wave\text{-}interaction} + \underbrace{\zeta_z[\nabla \times (\mathbf{v}' \times \boldsymbol{\zeta})]_z}_{(b)\ perturbation\text{-}interaction} \underbrace{\qquad}_{(c)\ buoyancytorque} + \underbrace{\zeta_z[\nu \nabla^2 \boldsymbol{\zeta}]_z}_{(d)\ viscosity}, \tag{9c}$$

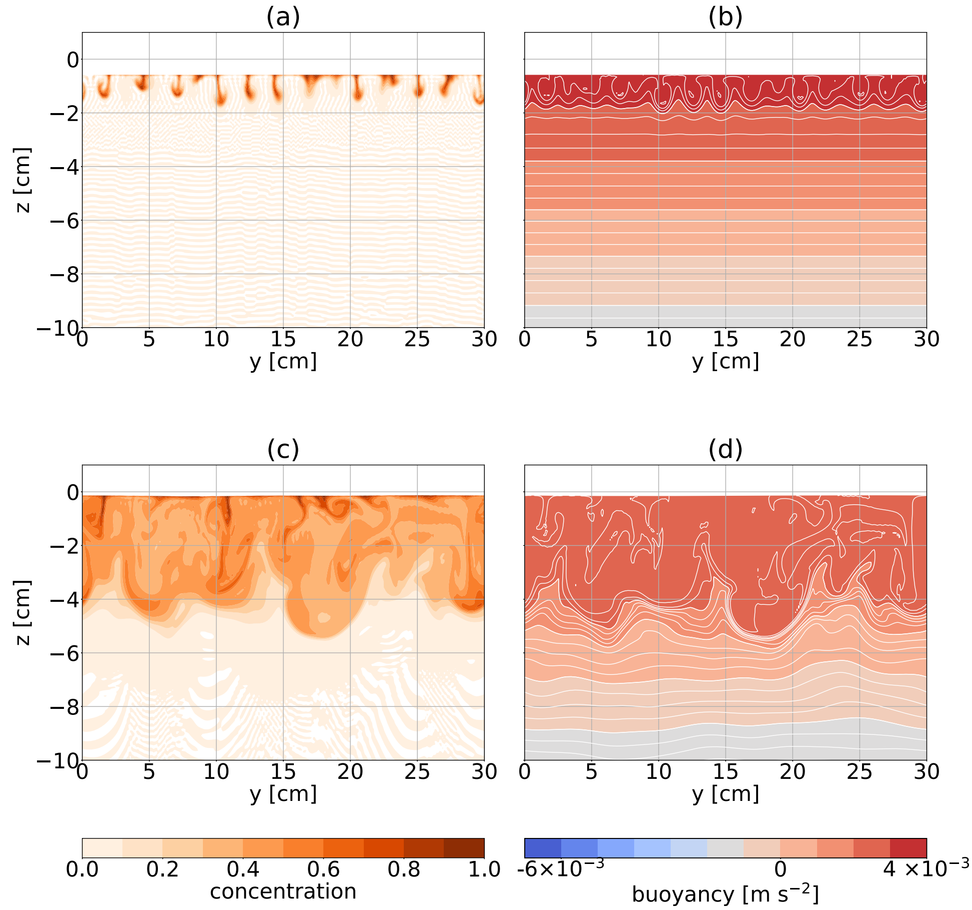

Fig. 6 Distributions of the tracer concentration d (a and c) and the buoyancy b (b and d) in y-z section at $x = 0.5\ \lambda$ at $t = 70\ T_w$ (a and b, near the end of the growing stage) and at $t = 560\ T_w$ (c and d, mature stage). The primary wave propagates normal to the page (out)

In the above equations, velocity $\mathbf{v}$ on the right hand side is decomposed into $\tilde{\mathbf{v}}$ [the primary and secondary surface waves (SWs) component] and $\mathbf{v}'$ (the perturbation component including vortex pairs) defined by Eqs. 7 and 8. Here the wavenumber spectral decomposition was done along constant z. The first (second) terms on the right hand side represent the interaction between the SWs (perturbation) component velocity and vorticity. These interaction terms include the advection, tilting, and stretching or shrinking of the vorticity by each velocity component. The third terms in Eqs. 9a and 9b are the buoyancy torque. The last terms in Eq. 9 represent the viscous diffusion and dissipation. Hereafter, these terms are referred to as the wave-interaction, perturbation-interaction, buoyancy torque, and viscosity, respectively.

Here we describe a roadmap of our enstrophy analysis. If the vortex pairs are generated locally through the LI mechanism, the wave-interaction terms should be dominant in each enstrophy budget equation [Eqs. 9a-9c]. On the other hand, if the vortex pairs are caused by the CL2 mechanism as in LCs, the vorticity is produced and intensified by the following three steps (see also Fig. 8). In the first step (Fig. 8a), a vertically sheared streamwise flow, which has spanwise vorticity ζ_y, is induced. Under windless condition, the shear flow could be generated by the VWS due to the wave viscous attenuation (Tsai et al. 2017; Fujiwara et al. 2020), and the viscosity is expected to dominate the $\zeta_y^2/2$ budget equation [Eq. 9b]. In the second step (Fig. 8b), the spanwise vorticity ζ_y is tilted by the streamwise vorticity ζ_x to produce the vertical vorticity ζ_z. This tilting is represented by the perturbation-interaction term in the $\zeta_z^2/2$ budget equation [Eq. 9c]. In the last step (Fig. 8c), the streamwise vorticity ζ_x is produced from the vertical vorticity ζ_z by rectified tilting owing to the wave-current interactions (e.g., Fujiwara et al. 2018). The tiling is expressed by the wave-interaction term in the $\zeta_x^2/2$ budget equation [Eq. 9a]. In the following, these three steps in the $\zeta_y^2/2$, $\zeta_z^2/2$, and $\zeta_x^2/2$ budget equations are examined in this order.

4.2.1 ζ_y^2 budget analysis

First, the $\zeta_y^2/2$ budget analysis is performed to examine the above first step (Fig. 8a). Figure 9 shows the vertical profiles of the xy-averaged terms (Figs. 9a,b) at t =

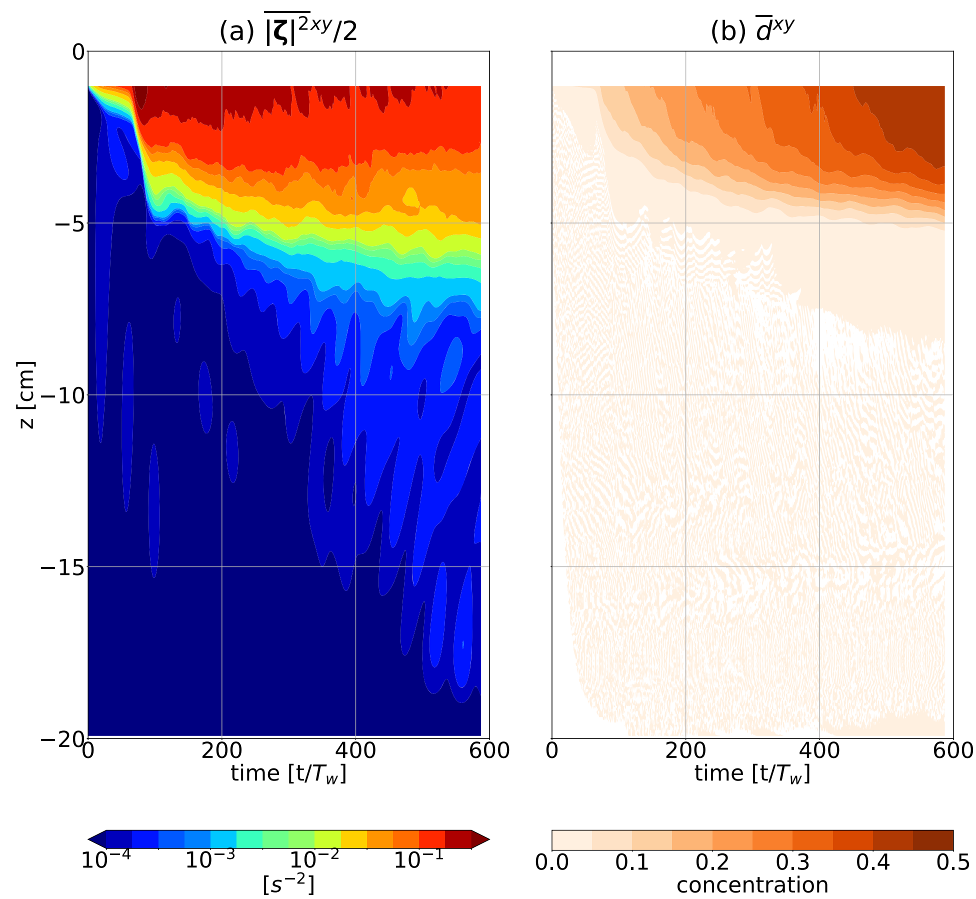

Fig. 7 Temporal evolutions of the vertical profiles of xy-averaged (a) enstrophy $\overline{|\boldsymbol{\zeta}|^2}^{xy}/2$ and (b) tracer concentration $\overline{d}^{xy}$. The horizontal axis shows time normalized by the wave period of the primary wave

70 T_w (near the end of growing stage) and 560 T_w (mature stage) and temporal change of the terms in the $\zeta_y^2/2$ budget equation [Eq. 9b] averaged over the high enstrophy region ($\overline{|\boldsymbol{\zeta}^2|}^{xy}/2 > 10^{-2}$ s^{-2}) (Fig. 9c). The budget terms in the following analysis were first evaluated at every $T_w/10$ and then averaged over T_w. Both at $t = 70\ T_w$ (averaged over $69.5\ T_w \leq t < 70.5\ T_w$; Fig. 9a) and $t = 560\ T_w$ (Fig. 9b), the perturbation-interaction (orange line) increases ζ_y^2 while the viscosity (red line) decreases it. The wave-interaction (blue line) is as large as the above two terms but changes sign with depth, whereas the buoyancy torque (green line) is almost zero. At $t = 560\ T_w$ (Fig. 9b), all terms penetrate to a greater depth, corresponding to the deepening destratification, and become smaller than at $t = 70\ T_w$ (Fig. 9a). The wave-interaction term averaged over the high enstrophy region (Fig. 9c) is negative at the beginning of the simulation and then becomes small, which is in marked contrast to what is expected from the LI mechanism. The averaged viscosity

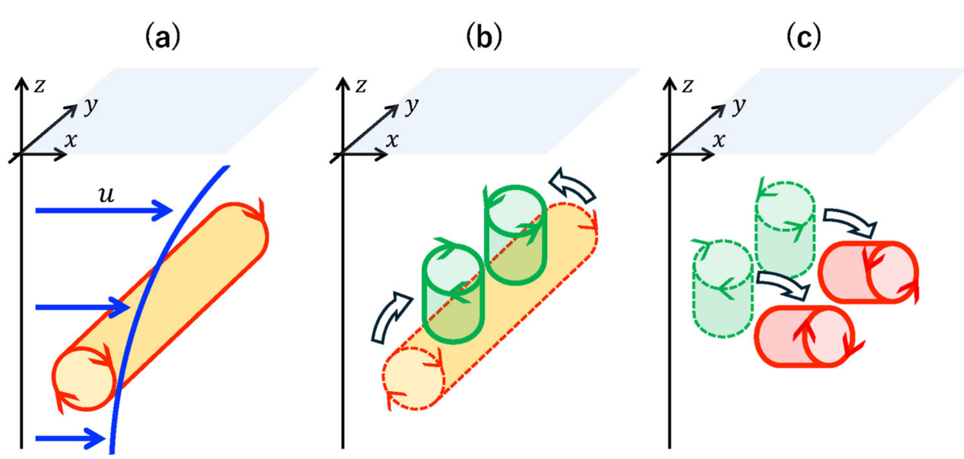

Fig. 8 Conceptual sketch showing three steps by which the vorticity is produced and intensified via the CL2 mechanism. Cylinders show vorticity. Blue arrows and curve in Panel a represent vertically sheared streamwise flow and its vertical profile. Unshaded arrows in Panels b and c indicate the tilting up and down of the vorticity

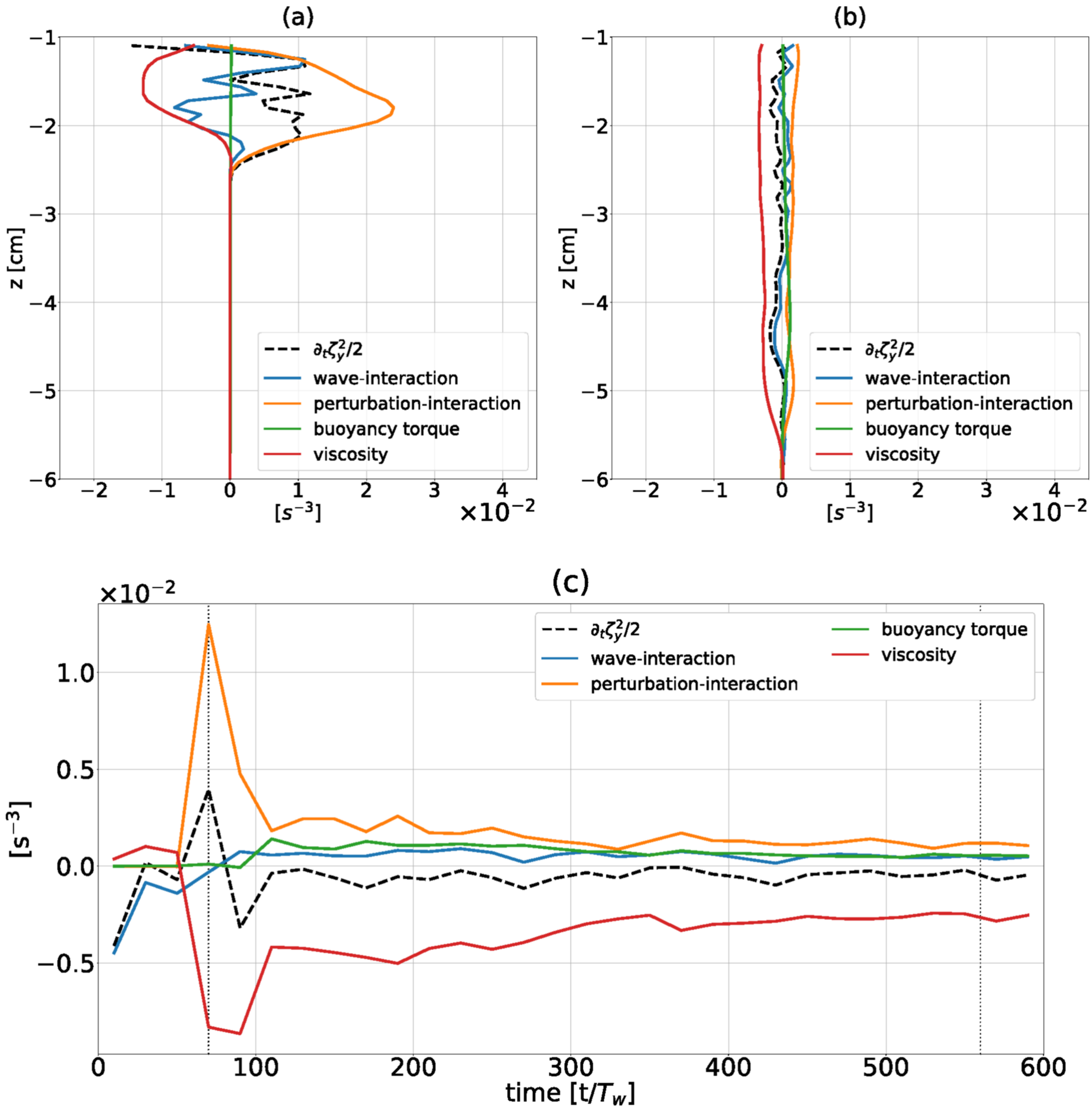

Fig. 9 Budget analysis of $\zeta_y^2/2$ based on Eq. 9b. (a), (b): Vertical profiles of xy-averaged terms in Eq. 9b at (a) $t = 70\ T_w$ (growing stage) and (b) $t = 560\ T_w$ (mature stage). (c): Temporal changes of the terms in Eq. 9b averaged over the high enstrophy region ($\overline{|\boldsymbol{\zeta}^2|}^{xy}/2 > 10^{-2}\ \mathrm{s}^{-2}$). The horizontal axis shows time normalized by the wave period of the primary wave and vertical dotted lines indicate $t = 70\ T_w$ and 560 T_w

is the dominant production term at the beginning of the simulation ($t < 50\ T_w$), as expected from the CL2 mechanism, but it turns to be the dominant reduction term throughout the rest of the simulation. After $t = 50\ T_w$, the averaged perturbation-interaction term (orange line) becomes the dominant production term.

Distributions of the $\zeta_y^2/2$ and its budget terms on the horizontal wavenumber space (k_x, k_y) better clarify roles played by the perturbation-interaction and the viscosity in more detail. Figures 10 and 11 show the distributions at $t = 70\ T_w$ and 560 T_w, respectively. The buoyancy torque term is not displayed because of its small magnitude. At $(k_x, k_y) =$

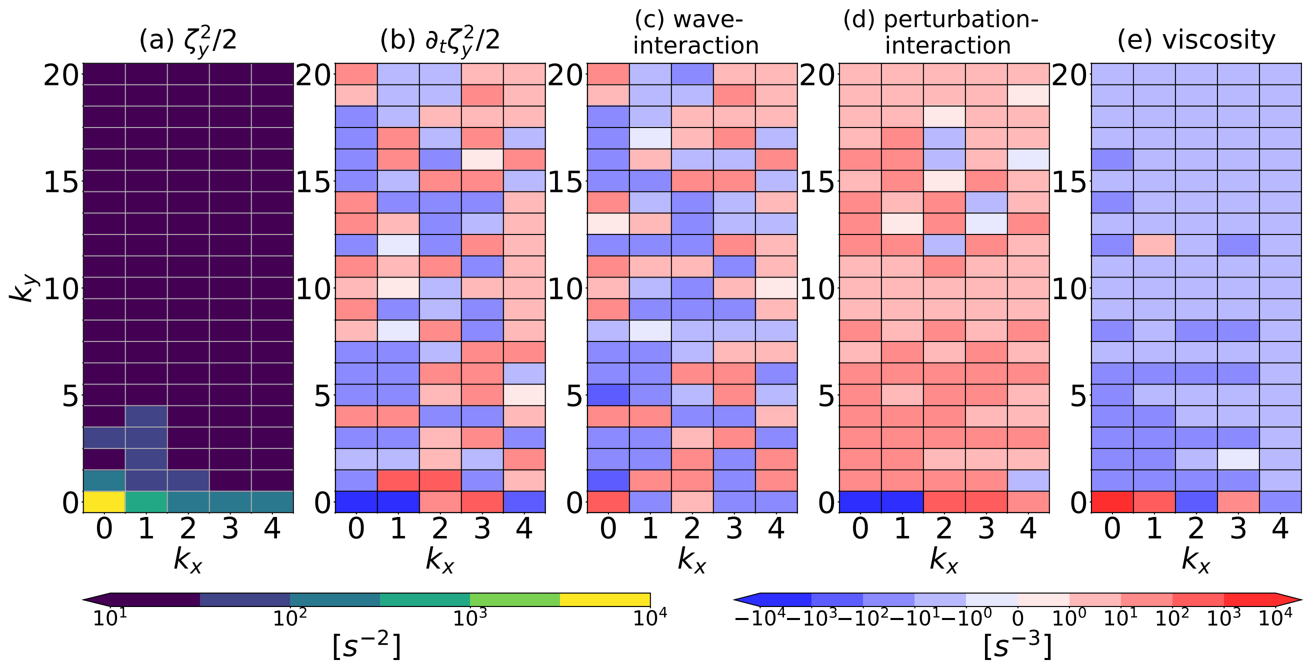

Fig. 10 Horizontal wavenumber ($0 \leq k_x \leq 4$, $0 \leq k_y \leq 20$) distributions of (a) $\zeta_y^2/2$, (b) its tendency term, (c) wave-interaction, (d) perturbation-interaction, and (e) viscosity terms in Eq. 9b at $z = -1$ cm at $t = 70\ T_w$ (growing stage). The lower-left color bar is for Panel a, and the lower-right color bar is for Panels b-e

(0, 0), $\zeta_y^2/2$ is largest at $t = 70\ T_w$ (Fig. 10a) and is still large and grows in magnitude at $t = 560\ T_w$ (Figs. 11a,b). At that wavenumber, the viscosity term is positive, indicating that the viscosity at $(k_x, k_y) = (0, 0)$, or horizontally averaged viscosity, generates $\zeta_y^2/2$ throughout the simulation (Figs. 10e and 11e). The perturbation-interaction term is negative at $(k_x, k_y) = (0, 0)$ and positive at other wavenumbers, indicating redistribution of $\zeta_y^2/2$ to a higher spanwise wavenumber (k_y) region (Figs. 10d and 11d). In this higher wavenumber region, the viscosity term is negative, indicating that the $\zeta_y^2/2$ is reduced by the viscosity. The $\zeta_y^2/2$ at $(k_x, k_y) = (0, 0)$, or horizontally averaged $\zeta_y^2/2$, corresponds to the vertical

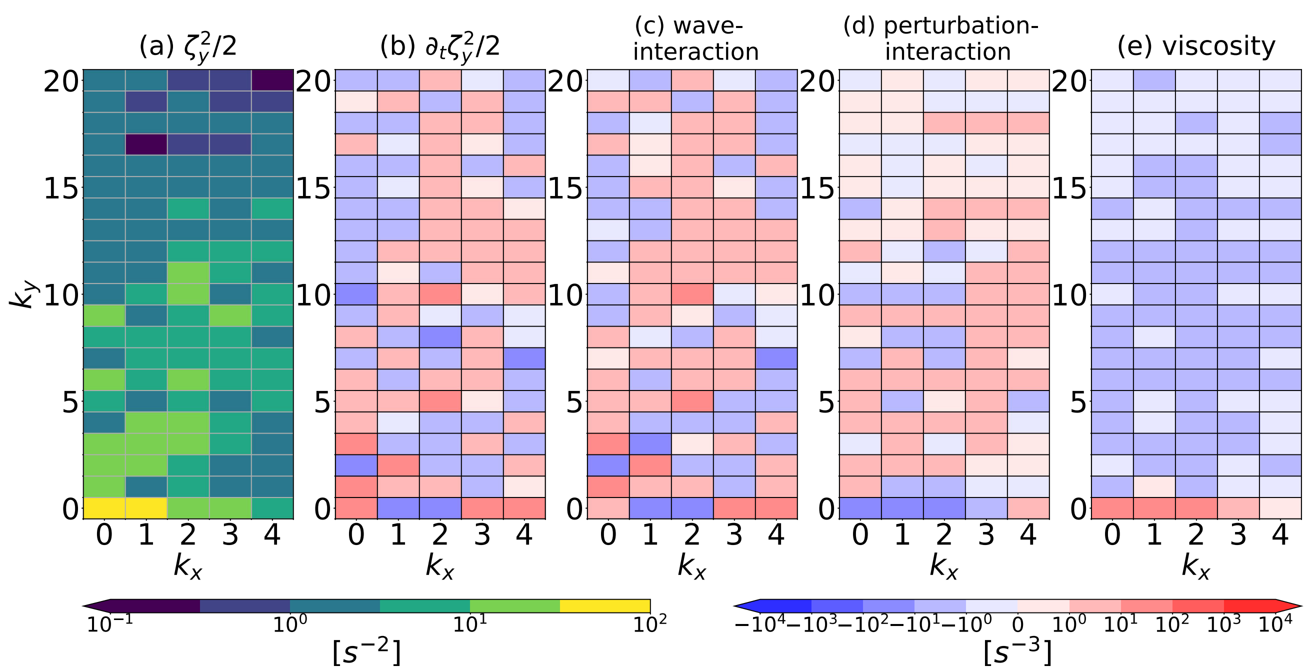

Fig. 11 Same as Fig. 10, but at $t = 560\ T_w$ (mature stage)

shear of the xy-averaged streamwise velocity $\overline{u}^{xy}$. A comparison with the results of the vertical one-dimensional diffusion equation ($\partial_t u = \nu \partial_z^2 u$), with VWS estimated from the wavelength and amplitude of the primary wave clarifies that the horizontally averaged $\zeta_y^2/2$ is produced by the VWS (see Appendix A for more detail). The high $\zeta_y^2/2$ near the surface is transported to a greater depth primarily by the perturbation-interaction term (Figs. 9a,b, mainly via vertical advection), where the viscosity reduces $\zeta_y^2/2$. Negative value of the horizontal sum of the viscosity term indicates that this reduction corresponds to dissipation of the $\zeta_y^2/2$.

4.2.2 ζ_z^2 budget analysis

Next, the ζ_z^2 budget is analyzed to see the second step of our enstrophy analysis (Fig. 8b). Figures 12-14 are the same as Figs. 9-11 except for $\zeta_z^2/2$ terms instead of $\zeta_y^2/2$ terms.

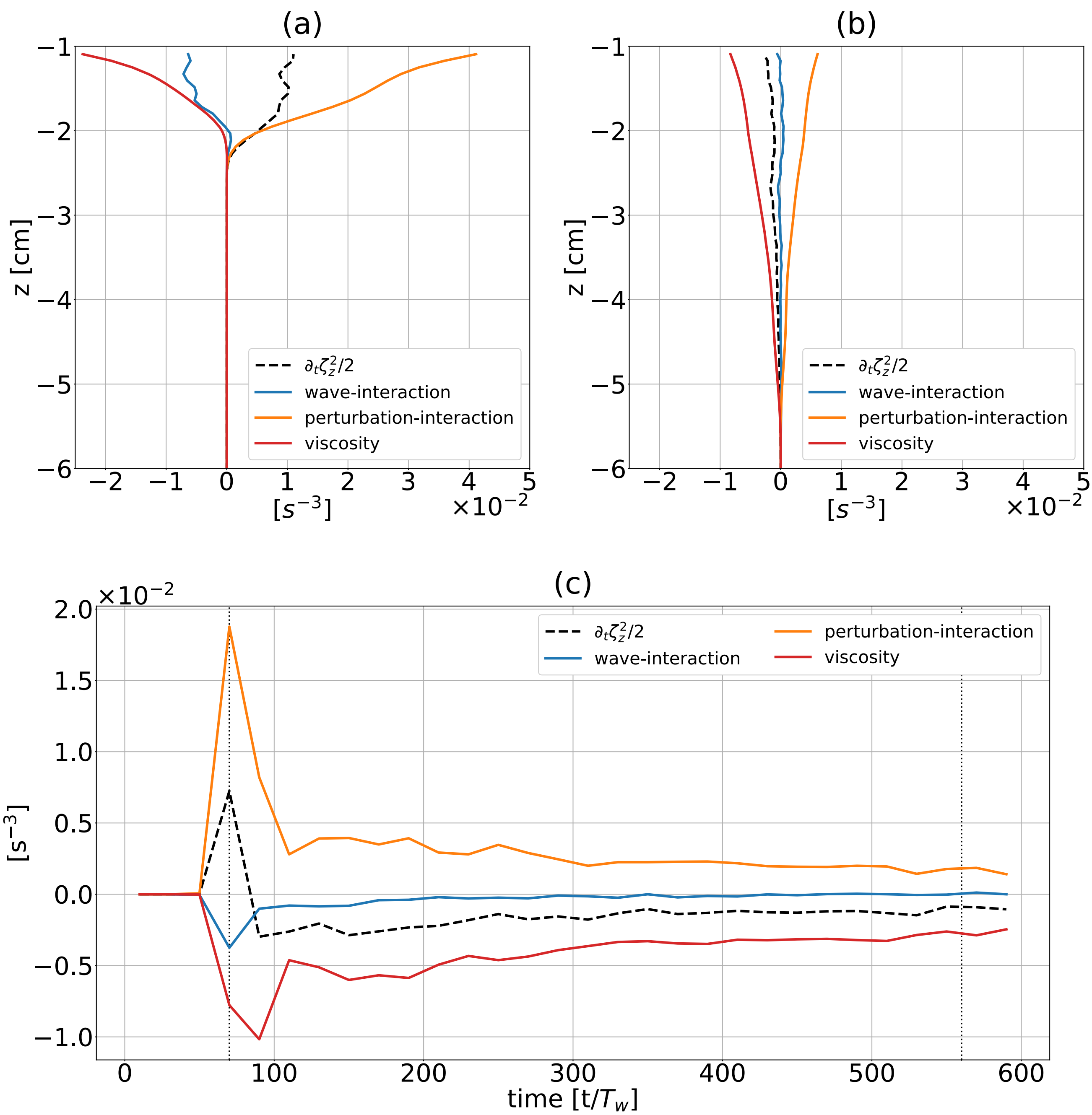

Fig. 12 Same as Fig. 9 but for $\zeta_z^2/2$

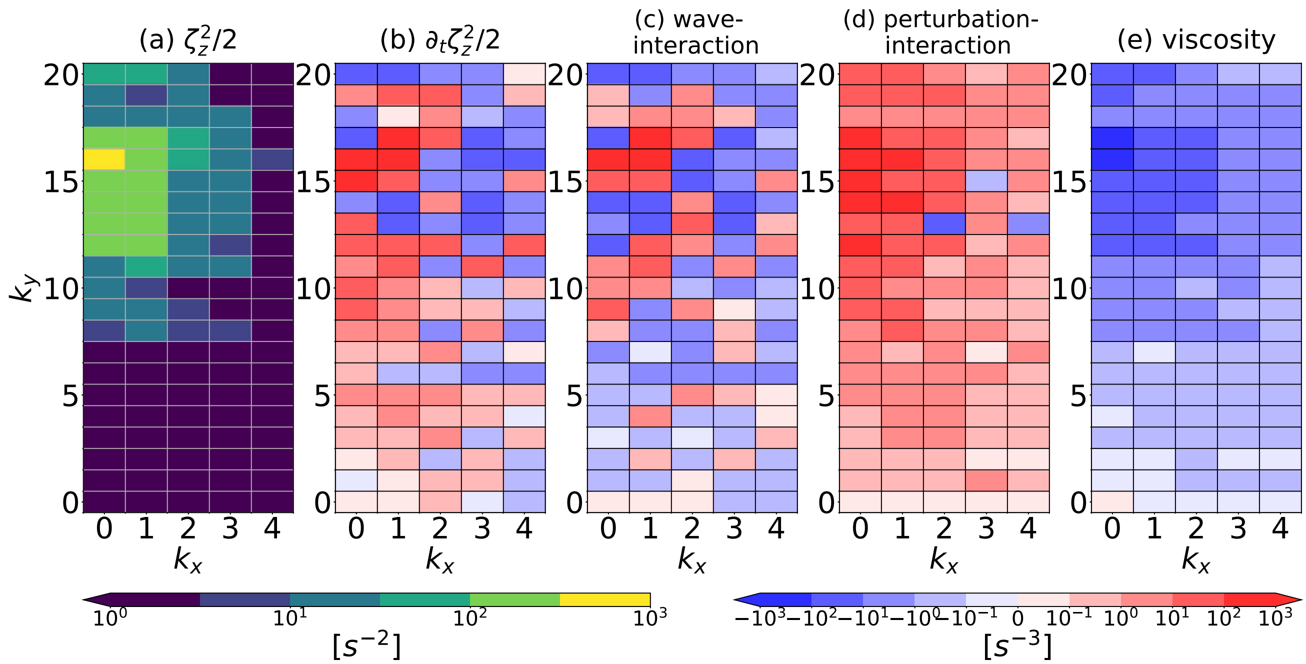

Fig. 13 Same as Fig. 10 but for $\zeta_z^2/2$

The perturbation-interaction term (orange line in Fig. 12), the term working in the CL2 mechanism, dominates the production of $\zeta_z^2/2$ at each depth at both $t = 70\ T_w$ (Fig. 12a) and $t = 560\ T_w$ (Fig. 12b). It keeps producing $\zeta_z^2/2$ in the high enstrophy region throughout the simulation (Fig. 12c). The wave-interaction term (blue line), corresponding to the LI mechanism, reduces $\zeta_z^2/2$ in the growing stage and has little contribution to the budget in the mature stage. The viscosity (red line) works to reduce (dissipate) the $\zeta_z^2/2$. From a wavenumber space perspective (Figs. 13 and 14), $\zeta_z^2/2$ around its peak wavenumbers is produced by the perturbation-interaction term.

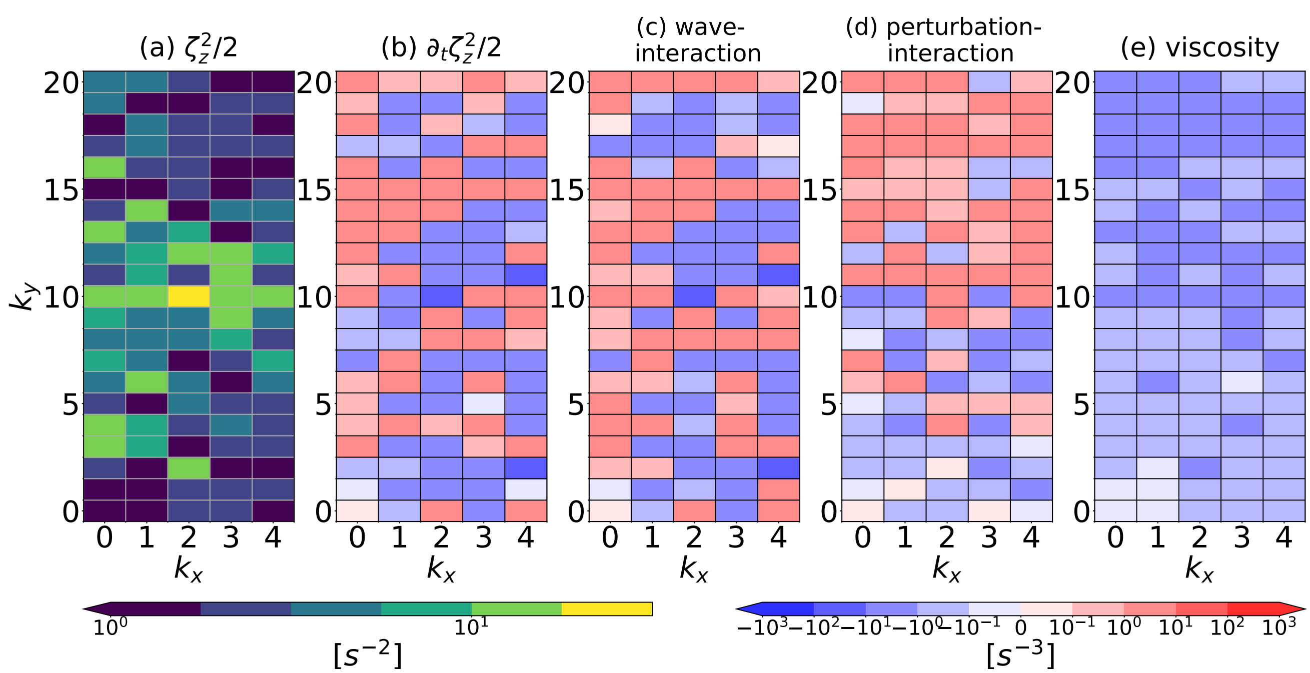

Fig. 14 Same as Fig. 11 but for $\zeta_z^2/2$

We further discuss the production by the perturbation-interaction $\zeta_z[\nabla \times (\mathbf{v}' \times \boldsymbol{\zeta})]_z$. This term comprises the following six terms:

$$\zeta_z[\nabla \times (\mathbf{v}' \times \boldsymbol{\zeta})]_z = \underbrace{-\partial_x(u'\frac{\zeta_z^2}{2}) - \partial_y(v'\frac{\zeta_z^2}{2})}_{horizontal\ advection} \underbrace{-\partial_z(w'\frac{\zeta_z^2}{2})}_{vertical\ advection}$$

$$+ \underbrace{\zeta_z\zeta_x\partial_x w'}_{x\text{-}to\text{-}z\ tilting} + \underbrace{\zeta_z\zeta_y\partial_y w'}_{y\text{-}to\text{-}z\ tilting}$$

$$+ \underbrace{\zeta_z\zeta_z\partial_z w'}_{stretching\ or\ shrinking} . \quad (10)$$

As mentioned before, this term includes advection, tilting, and stretching or shrinking. If the CL2 mechanism works,

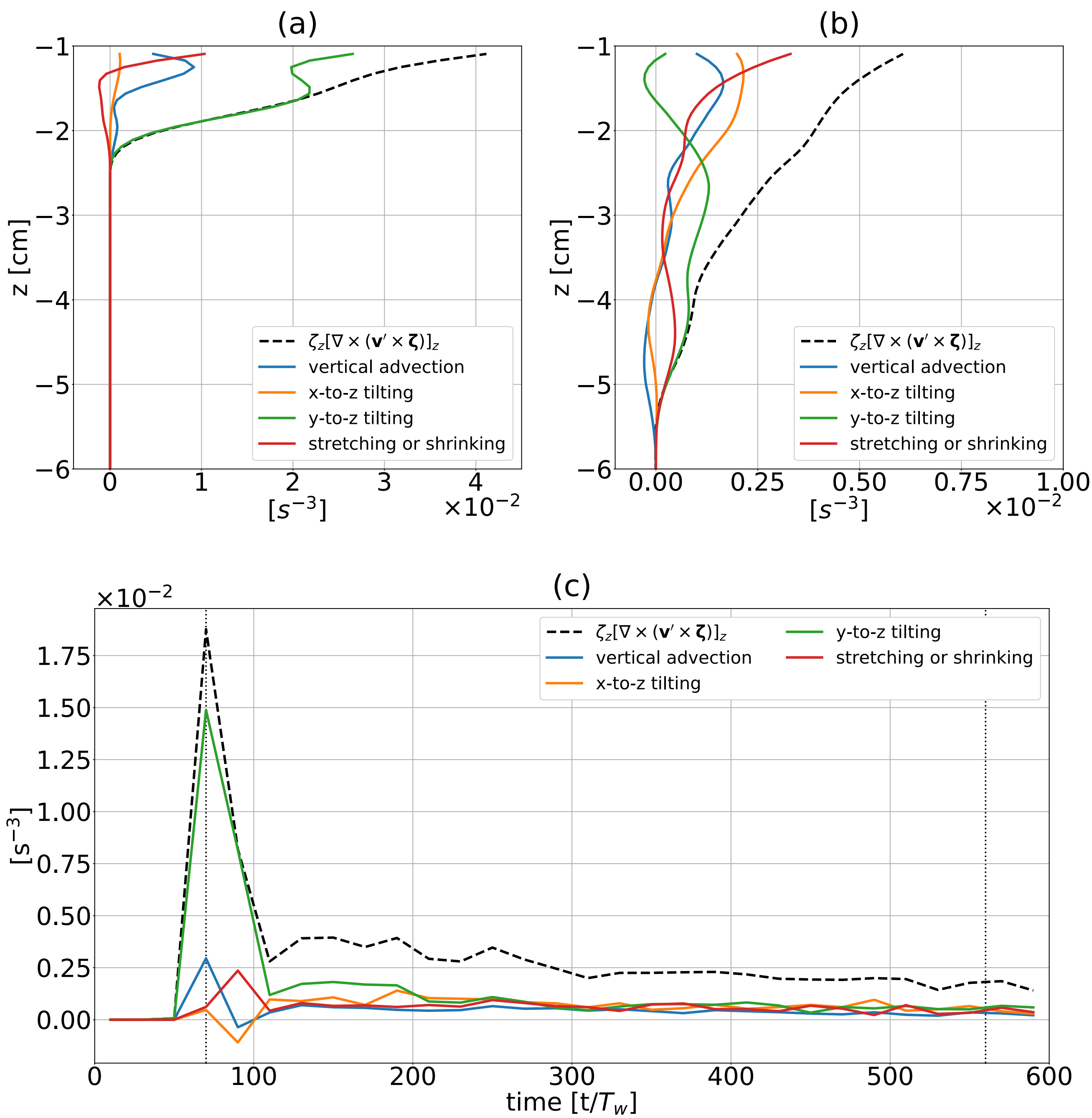

Fig. 15 The terms comprising the perturbation-interaction term in the $\zeta_z^2/2$ budget equation ($\zeta_z[\nabla\times(\mathbf{v}'\times\boldsymbol{\zeta})]_z$) [Eq. 10]. (a),(b): Vertical distributions of xy-averaged terms in Eq. 10 at (a) $t = 70\ T_w$ (growing stage) and (b) $t = 560\ T_w$ (mature stage). (c): Temporal changes of the terms in Eq. 10 averaged over the high enstrophy region ($\overline{|\boldsymbol{\zeta}^2|}^{xy}/2 > 10^{-2}\ \mathrm{s}^{-2}$). The horizontal axis shows time normalized by the wave period of the primary wave and vertical dotted lines indicate $t = 70\ T_w$ and 560 T_w

the y-to-z tilting term should be dominant. Figure 15 shows the vertical profiles of the xy-averaged terms in Eq. 10 at $t = 70\ T_w$ and $t = 560\ T_w$ (Figs. 15a,b) and the temporal changes of the terms averaged over the high enstrophy ($\overline{|\zeta^2|}^{xy}/2 > 10^{-2}\ \mathrm{s}^{-2}$) region (Fig. 15c). In the growing stage, the y-to-z tilting (green line) dominates (Figs. 15a,c). In the mature stage, the y-to-z tilting continues to work whereas other processes, such as x-to-z tilting (orange line) which may be associated with the undulation of the streamwise vortex pairs (Figs. 4b,d,f,h), also contribute to intensifying $\zeta_z^2/2$.

4.2.3 ζ_x^2 budget analysis

Lastly, the ζ_x^2 budget is analyzed for the last step of the enstrophy analysis (Fig. 8c). Figure 16 shows $\zeta_x^2/2$ budget terms as Fig. 9 does. At $t = 70\ T_w$ (Fig. 16a) and $t = 560\ T_w$ (Fig. 16b), the wave-interaction term (blue line in Fig. 16), which expected to work both in the LI and CL2 mechanism, mostly dominates $\zeta_x^2/2$ production at each depth. It keeps producing $\zeta_x^2/2$ dominantly in the high enstrophy region throughout the simulation (Fig. 16c).

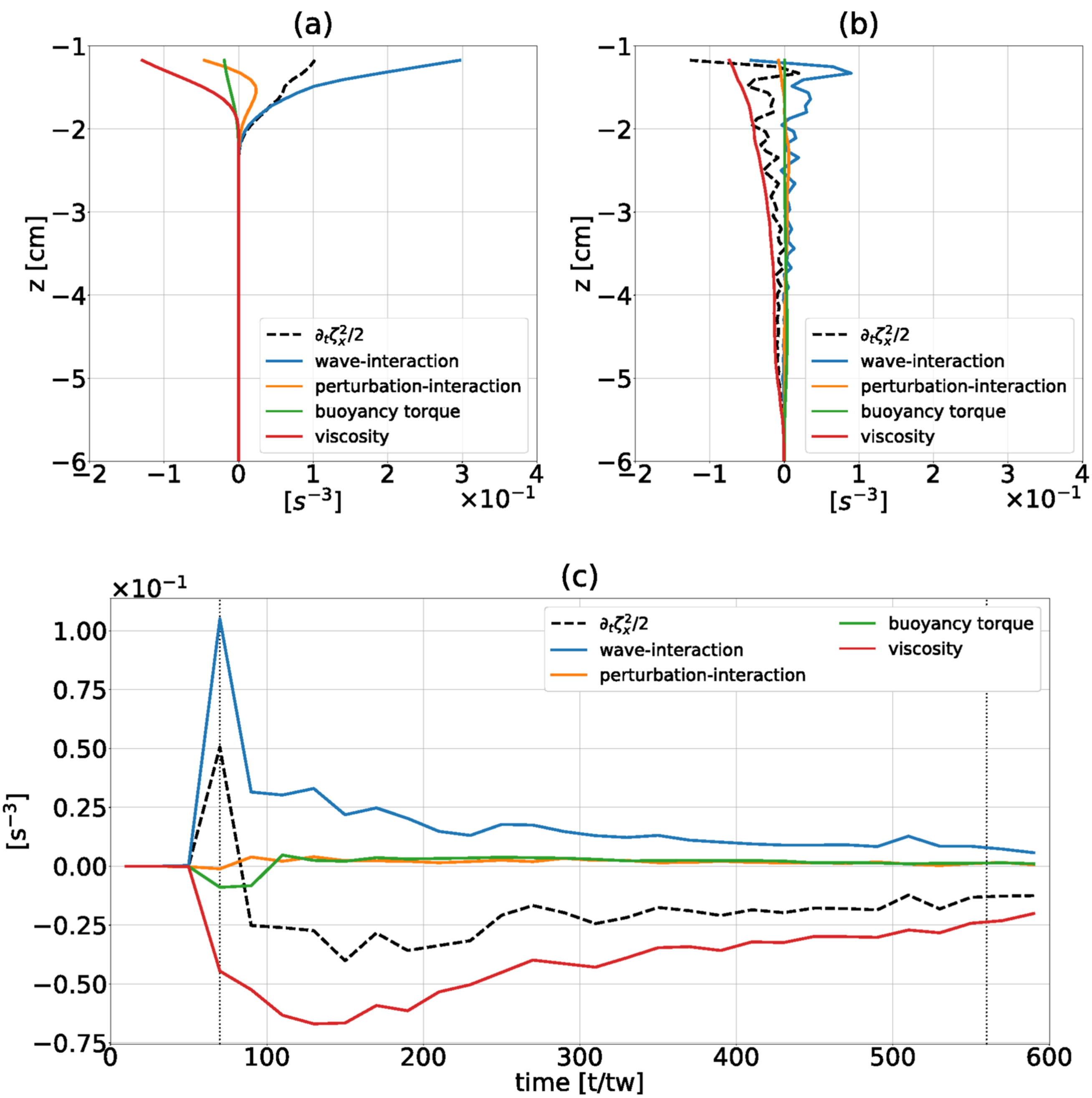

Fig. 16 Same as Fig. 9 but for $\zeta_x^2/2$

The wave-interaction term comprises the following five terms:

$$\zeta_x[\nabla \times (\tilde{\mathbf{v}} \times \boldsymbol{\zeta})]_x = \underbrace{-\partial_x(\tilde{u}\frac{\zeta_x^2}{2}) - \partial_y(\tilde{v}\frac{\zeta_x^2}{2})}_{horizontal\ advection} \underbrace{-\partial_z(\tilde{w}\frac{\zeta_x^2}{2})}_{vertical\ advection} + \underbrace{\zeta_x\zeta_x\partial_x\tilde{u}}_{stretching\ or\ shrinking} + \underbrace{\zeta_x\zeta_z\partial_z\tilde{u}}_{z\text{-}to\text{-}x\ tilting}. \tag{11}$$

Fujiwara et al. (2018) showed that the last three terms on the right-hand side of Eq. 11 converted the vertical vorticity ζ_z into streamwise vorticity ζ_x in their simulated LCs. Figure 17 shows the vertical profiles of the xy-averaged terms in Eq. 11 at $t = 70\ T_w$ (Fig. 17a) and $t = 560\ T_w$ (Fig. 17b) and the temporal changes of the terms averaged over the high enstrophy region (Fig. 17c). The vertical advection (blue line) and the stretching or shrinking (orange line) are positive, whereas the z-to-x tilting term (green line) is negative at $t = 70\ T_w$

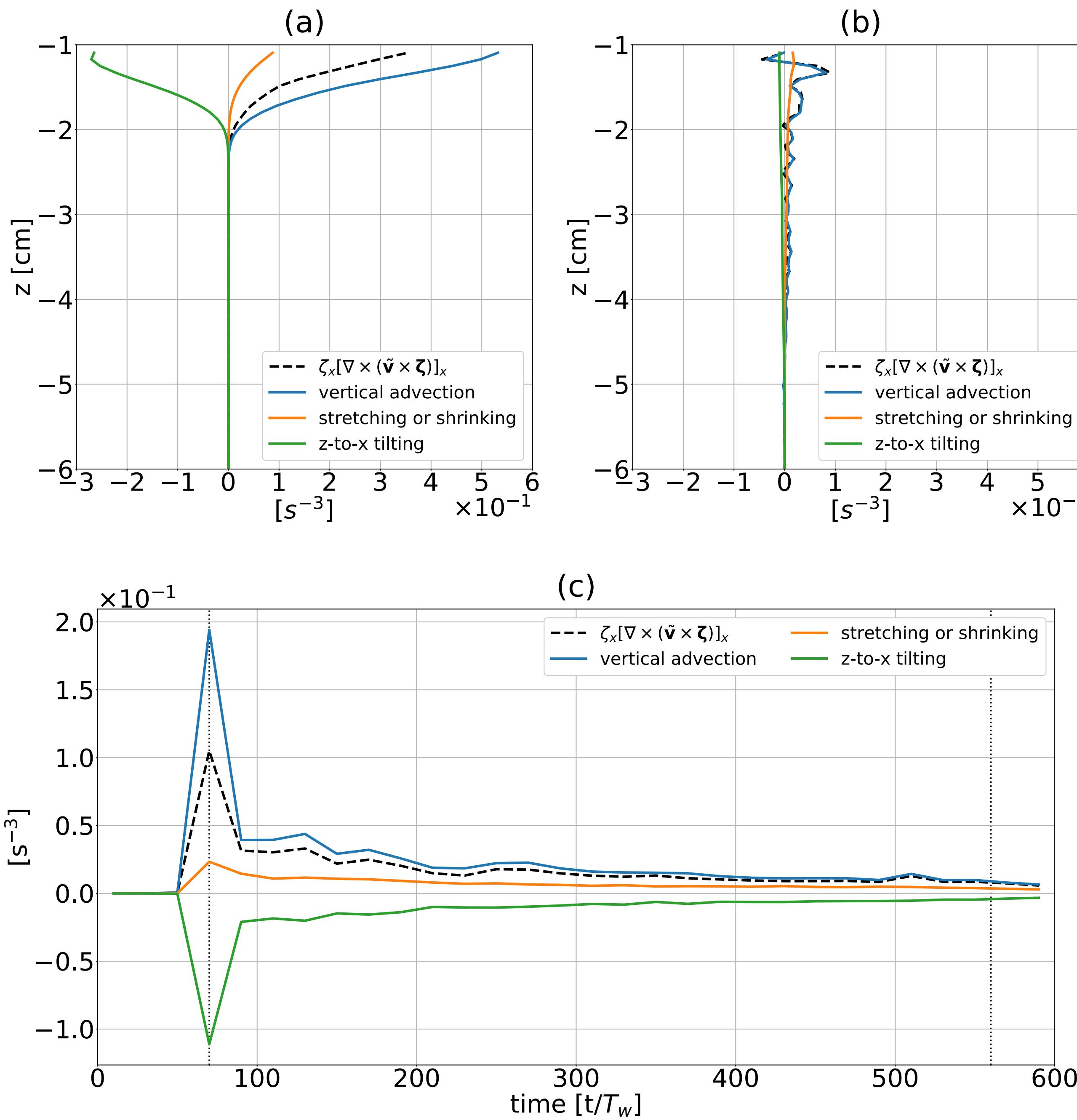

Fig. 17 Same as Fig. 15 but for the wave-interaction term in the $\zeta_x^2/2$ budget equation ($\zeta_x[\nabla \times (\tilde{\mathbf{v}} \times \boldsymbol{\zeta})]_x$) [Eq. 11]

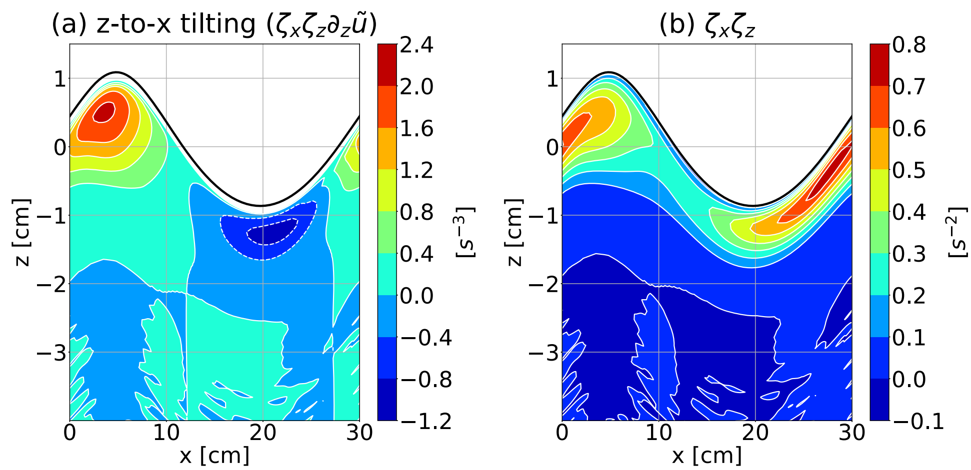

Fig. 18 Distributions of the y-average of (a) z-to-x tilting term ($\zeta_x\zeta_z\partial_z\tilde{u}$) and (b) product between ζ_x and ζ_z in x-z section at $t = 70\ T_w$ (growing stage). The wave propagates from left to right

(Fig. 17a) and $t = 560\ T_w$ (Fig. 17b). This holds true for the high enstrophy region throughout the simulation (Fig. 17c). The negative z-to-x tilting contrasts with the result of Fujiwara et al. (2018), where it was positive. This difference comes from different vertical resolution; we analyzed the enstrophy budget with a smaller vertical grid spacing near the minimum water level ($z = -a$) than Fujiwara et al. (2018) where vorticity was analyzed with a larger vertical grid spacing ($5a$) at a greater depth (below $z = -2.5a$ where a is wave amplitude in their simulation). Figure 18 illustrates the distribution of the y-average of the z-to-x tilting term and product between ζ_x and ζ_z in the x-z plane at $t = 70\ T_w$. Clearly,

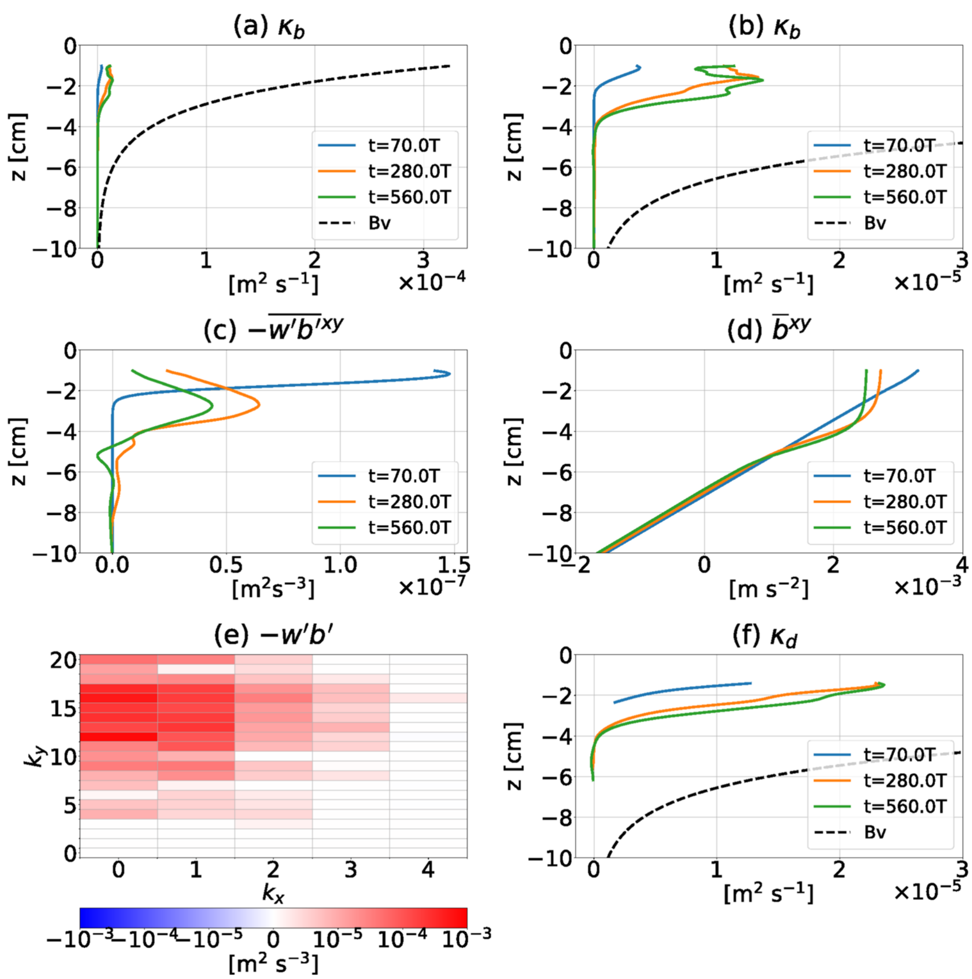

Fig. 19 (a)-(d), (f): Vertical profiles of (a), (b) buoyancy-based vertical eddy diffusivity [Panel b is the zoom of Panel a], (c) xy-averaged vertical buoyancy flux, (d) xy-averaged buoyancy, and (f) tracer-based vertical eddy diffusivity at $t = 70\ T_w$ (growing stage), $t = 280\ T_w$, and $t = 560\ T_w$ (mature stage). The tracer-based diffusivities are calculated using the vertically smoothed vertical flux $-\overline{w'd'}^{xy}$ and gradient $\partial_z\overline{d}^{xy}$ as in the buoyancy-based diffusivity. The profiles are depicted only the depth where $\partial_z d > 0.2\ \mathrm{m}^{-1}$. The black dashed lines in Panels a,b,f denote vertical distributions of parameterized eddy diffusivity B_v. (e): Horizontal wavenumber (k_x, k_y) distributions $(0 \le k_x \le 4,\ 0 \le k_y \le 20)$ of vertical buoyancy flux at $z = -1$ cm at $t = 70\ T_w$

Table 1 Wave parameters and experimental settings of the sensitivity tests

EXP	λ [cm]	a [cm]	ak	$L_x \times L_y$	h [cm]	$N_x \times N_y \times N_z$	Δt [s]	Integration Time
0	30	1.0	0.2	λ × λ	20	256×256×256	$T_w/200$	200 T_w
1	30	0.5	0.1	λ × λ	20	256×256×256	$T_w/200$	600 T_w
2	30	1.5	0.3	λ × λ	20	256×256×256	$T_w/200$	200 T_w
3	13	0.4	0.2	λ × λ	8.6	128×128×128	$T_w/200$	250 T_w
4	62	2.0	0.2	λ × λ/2	41	512×256×512	$T_w/300$	200 T_w
5	13	0.4	0.2	2λ × 2λ	8.6	256×256×128	$T_w/200$	250 T_w

Here, L_x and L_y indicate the x- and y-dimension of the computational domain, and N_x, N_y, and N_z represent the numbers of grid points in x-, y-, and z-direction respectively

z-to-x tilting is positive (negative) just below the wave crest (trough) (Fig. 18a). It is because ζ_x and ζ_z are positively correlated and their products are concentrated immediately beneath the surface (Fig. 18b). Our enstrophy analysis, performed below $z = -a$, captures only the negative z-to-x tilting. The $\zeta_x^2/2$ produced by the positive z-to-x tilting term above $z = -a$ is transported downward below $z = -a$ by the vertical advection (blue line in Fig. 17) Thus in total the above budget terms are consistent with those in Fujiwara et al. (2018) and the CL2 mechanism. Note also that the above

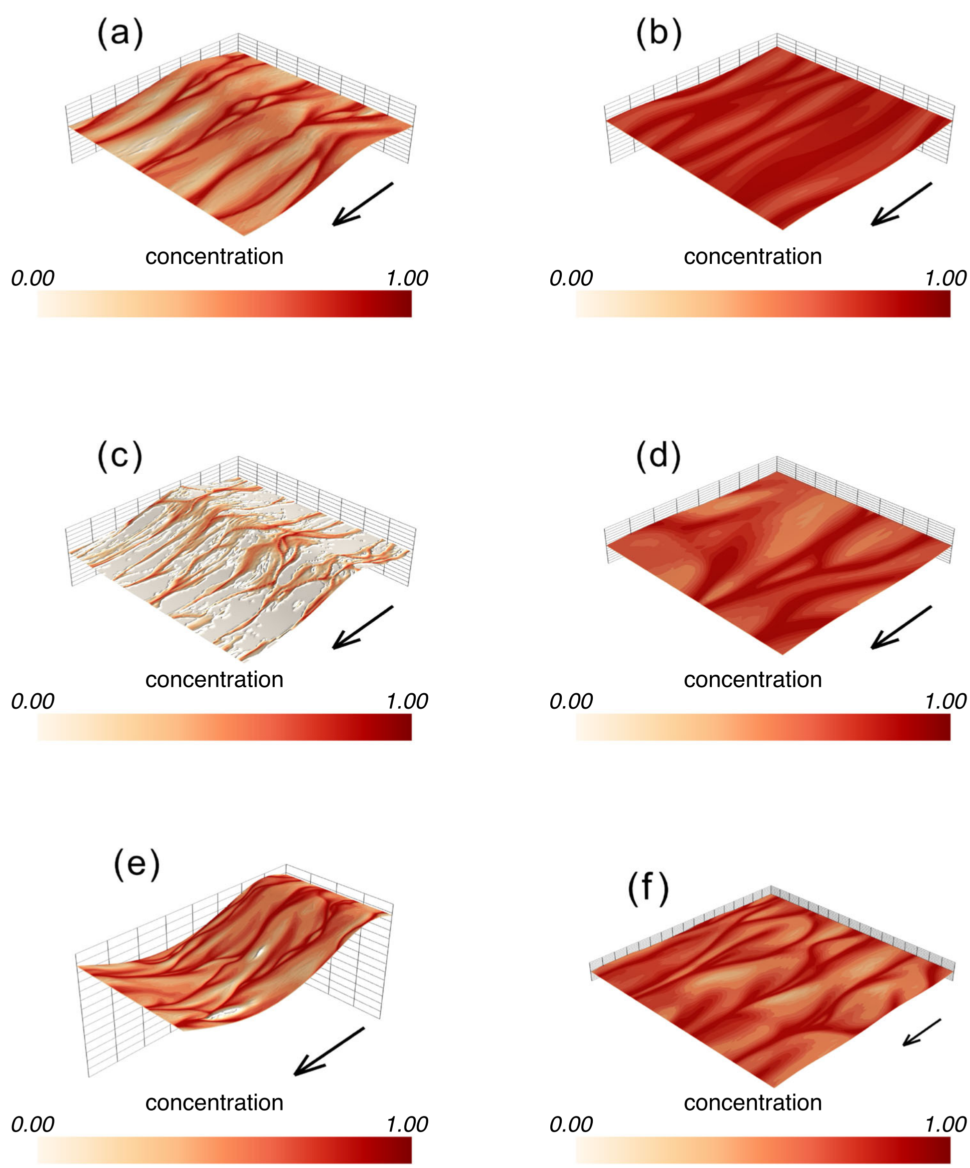

Fig. 20 Near-surface (z^*=0.998), mature stage distributions of tracer concentration d in the simulations (a) EXP 0 at $t = 175\ T_w$, (b) EXP 1 at $t = 500\ T_w$, (c) EXP 2 at $t = 130\ T_w$, (d) EXP 3 at $t = 215\ T_w$, (e) EXP 4 at $t = 175\ T_w$, and (f) EXP 5 at $t = 215\ T_w$. The primary waves of each experiment propagate in the direction of the black arrow shown in each panel

contribution of the advection term indicates nonlocal (rather than local) generation of $\zeta_x^2/2$ at greater depth.

4.2.4 Summary

From these results, we conclude that the CL2 mechanism continuously works not only in the growing stage but also in the mature stage. In the mature stage, additional processes, such as x-to-z tilting by perturbed motion along the x direction, have some contributions. We expect that the CL2 mechanism will continue to dominate even after our experimental period ($t = 600T_w$) because the enstrophy budget achieved an almost steady state in the mature stage. On the other hand, we could not find a continuous generation of vorticity by the local interaction between the wave and

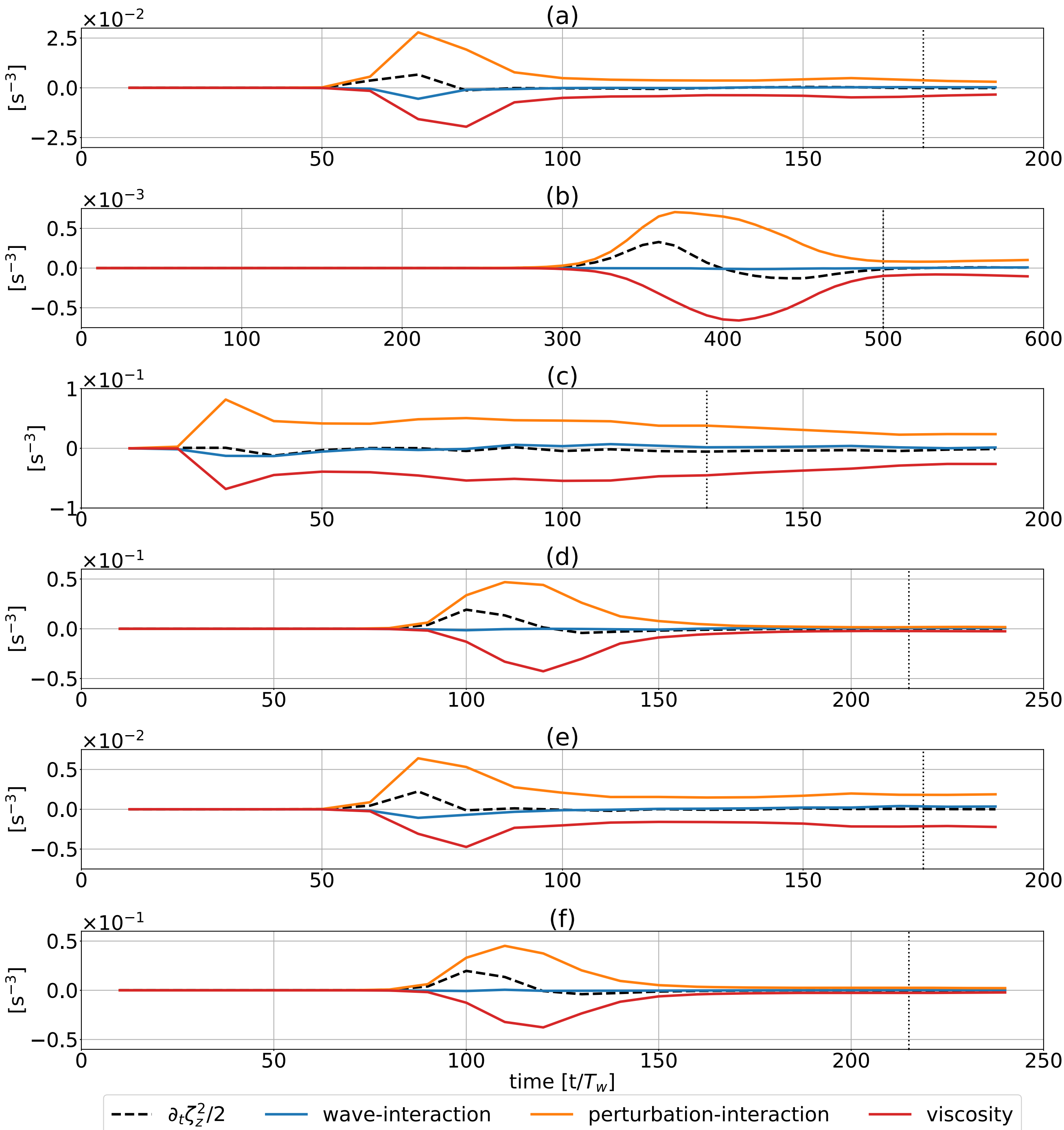

Fig. 21 Temporal changes of each of the terms in $\zeta_z^2/2$ budget equation [Eq. 9c] averaged over the high enstrophy ($\overline{|\zeta^2|}^{xy}/2 > 10^{-2}\ \mathrm{s}^{-2}$) region in the simulations (a) EXP 0, (b) EXP 1, (c) EXP 2, (d) EXP 3, (e) EXP 4, and (f) EXP 5 in Table 1

turbulence. Thus, the LI mechanism did not work in this experiment.

4.3 Eddy diffusivity

The simulated mixing intensity is quantified by the vertical eddy diffusivity κ_b defined as

$$\kappa_b = -\frac{\overline{w'b'}^{xy}}{\partial_z \overline{b}^{xy}}. \tag{12}$$

The vertical eddy diffusivity κ_b, vertical buoyancy flux $-\overline{w'b'}^{xy}$ and xy-averaged buoyancy $\overline{b}^{xy}$ are shown in Fig. 19. The buoyancy flux (Fig. 19c) and the averaged buoyancy (Fig. 19d) are vertically smoothed and then used to calculate the eddy diffusivity (Figs. 19a,b) to eliminate large fluctuation. Figures 19a and b show that the estimated eddy diffusivity is 3.7×10^{-6} m^2 s^{-1} at $t = 70\ T_w$ (blue line) and becomes 1.4×10^{-5} m^2 s^{-1} at $t = 560\ T_w$ (green line) which is two orders of magnitude greater than the molecular diffusivity. The buoyancy flux becomes slightly smaller but penetrates deeper with time (Fig. 19c) and the water is homogenized at greater depths (Fig. 19d) accordingly. The distribution of the vertical buoyancy flux on the horizontal wavenumber space (Fig. 19e) reveals that the buoyancy flux is large around the horizontal wavenumbers of the vortex pairs ($0 \leq k_x \leq 1, 9 \leq k_y \leq 17$ in Fig. 2), indicating that the vortex pairs cause mixing. The eddy diffusivities estimated from the tracer distribution (κ_d), used in the Section 5, are larger than those from buoyancy near the surface but quantitatively similar to the buoyancy-based diffusivities (Fig. 19f).

The dashed lines in Fig. 19a, b, and f display the parameterized eddy diffusivity B_υ used in Dai et al. (2010). As Fig. 19a shows, B_υ overestimates the simulated mixing. In addition, B_υ remains constant with time, whereas the simulated eddy diffusivity evolves. As described in the Section 4.2, mixing simulated in our experiments is induced not by locally generated turbulence through the LI mechanism but by vortex pairs generated primarily through the CL2 mechanism, which is not properly represented by B_υ.

5 Sensitivity test

To see robustness of the observed features in Section 4, sensitivities on water stratification, wave parameter, and

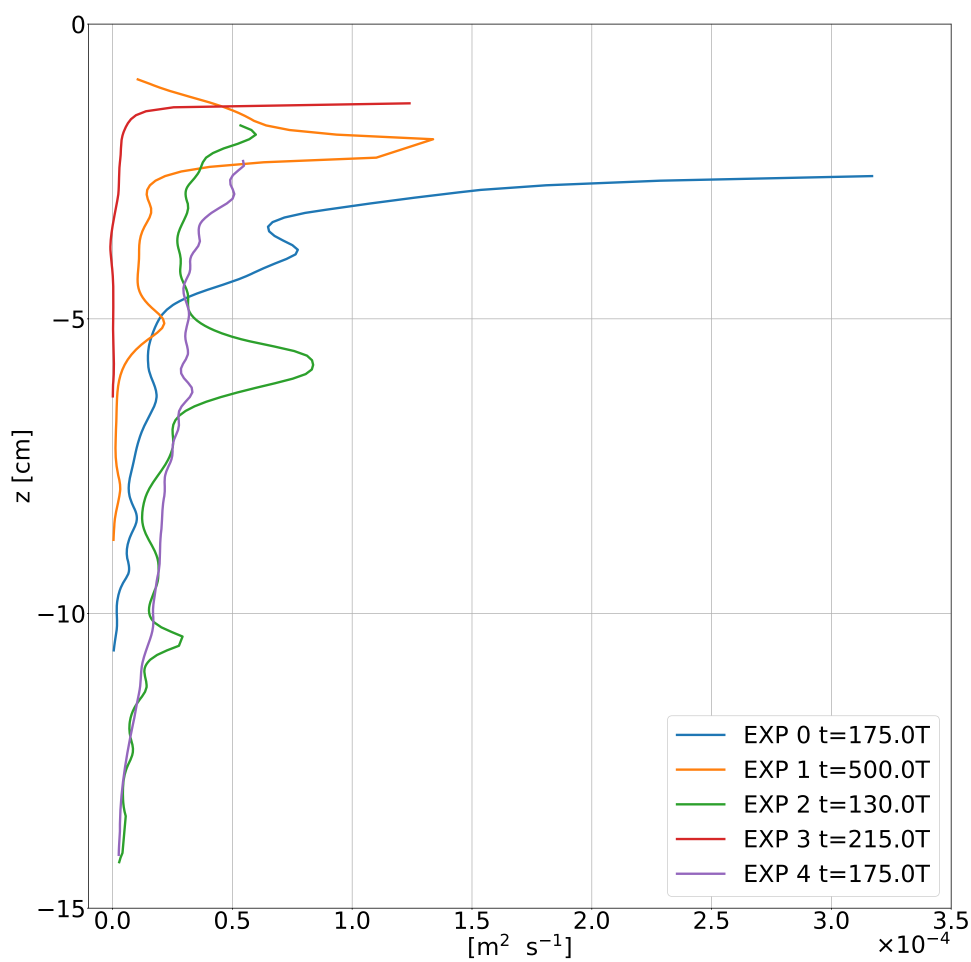

Fig. 22 Vertical profiles of tracer-based vertical eddy diffusivity κ_d in the mature stage in the simulations EXP 0, 1, 2, 3, and 4 in Table 1. The diffusivities are calculated using the vertically smoothed the vertical flux $-\overline{w'd'}^{xy}$ and gradient $\partial_z \overline{d}^{xy}$. The profiles are depicted only the depth where $\partial_z d > 0.2$ m^{-1}

computational domain are tested by six additional simulations (Table 1). Hereafter, the simulation described in Section 3 is referred to as the standard experiment.

5.1 Stratification

First, to see the stratification effects, a simulation without stratification was conducted (EXP 0 in Table1). Other experimental settings than the stratification and integration time are the same as those in the standard experiment.

Figure 20a displays the near-surface distributions of the passive tracer concentration d at $t = 175\ T_w$ (mature stage in this experiment). The streamwise streaks of the tracer corresponding to the vortex pairs are developed as in the standard experiment. It should be noted that the surface-integrated perturbation kinetic energy reaches at mature stage 10 T_w earlier than in the standard experiment, indicating that the stratification dampens the vortex growing in the standard experiment (not shown). Enstrophy budget analysis shows that relative contributions of the terms are similar to those in the standard experiment, indicating that the CL2 mechanism works (see for example budget terms in $\zeta_z^2/2$ equation, Fig. 21a). Eddy diffusivity estimated from the tracer concentration (κ_d) at the mature stage is shown in Fig. 22 (blue line) and its largest value is one order larger than that of standard experiment in the mature stage. These results suggest that stratification does not make qualitative changes in the generation mechanism of the vortex pairs and the turbulence mixing but has quantitative effects on mixing intensity.

5.2 Wave parameter

Second, we run simulations with four sets of wavelength and initial amplitude (EXP 1-4 in Table 1). The stratification was also removed as in EXP 0 to save computational time. The physical parameters and boundary conditions were set the same as those of the standard experiment. The streamwise dimension of the computational domain was set to λ, and the spanwise dimension was λ except for simulation EXP 4 where the spanwise dimension was $\lambda/2$ due to the limitation of computational resources. Still water depth was set to satisfy $kh = 4.2$, as in the standard experiment. The number of grid points was chosen to keep the grid spacings similar to those of the standard experiment. The simulations were conducted until the surface-integrated perturbation kinetic energy became statistically steady, with a time-step interval of $\Delta t = T_w/200$ except for the simulation EXP 4 where Δt was set as $T_w/300$ to ensure numerical stability.

In all the experiments, streaks elongated in the streamwise direction are observed in the near-surface tracer distributions (Figs. 20b-e) as well as the vortex pairs (not shown). The larger the wave steepness becomes, the earlier the simulated fields reaches at the mature stage (not shown). Enstrophy budget analysis reveals that the vortex pairs are generated via the CL2 mechanism, though the magnitudes of the terms vary among the experiments (see again, for example, budget terms in $\zeta_z^2/2$ equation, Figs. 21b-e). The largest values of the tracer-based vertical eddy diffusivity κ_d ranges from 5.0×10^{-5} to 1.3×10^{-4} m^{2}s^{-1} at mature stages, three orders larger than the molecular diffusivity (orange, green, red, and purple lines in Fig. 22). All profiles are different from the corresponding B_υ profile (not shown). Detailed dependence of the magnitude and profiles on the wave parameters are out of the scope of the present study. It is nevertheless confirmed that CL2 mechanism works and intensive mixing occurs in all test cases of the experiments.

5.3 Computational domain size

Lastly, to test the sensitivity of the computational domain size, simulation EXP 5 was conducted which is the same as simulation EXP 3 except that the domain size was twice enlarged in the x- and y-directions. The near-surface tracer distribution (Fig. 20f) and enstrophy budget (Fig. 21f) are similar to those in EXP3 (Figs. 20d and 21d). These results indicate that computational domain size does not affect the results.

6 Conclusion

In this study, we ran a DNS of nonbreaking surface-wave-induced mixing under windless condition (WL wave-induced mixing) which was modeled after a laboratory experiment with a 30 cm wavelength in Dai et al. (2010). We observe that water is destratified by the WL wave-induced mixing, as in Dai et al. (2010). The enstrophy budget analysis reveals that the CL2 mechanism, similar to Langmuir circulations, continues to work not only in the growing stage but also in the mature stage and induce mixing. The local generation of vorticity (turbulence) by the primary wave (LI mechanism) was not found in our simulation. This holds true for the wave with half or twice wavelength/amplitude propagating over unstratified water. The estimated vertical eddy diffusivity is $O(10^{-5}\ \mathrm{m}^2\ \mathrm{s}^{-1})$ at largest in our experiment, and its vertical profile and temporal change are different from that of parameterized vertical eddy diffusivity (B_υ), in which turbulence is assumed to be produced locally by the surface wave. Therefore, we conclude that the mixing simulated in our numerical experiment is induced not by the LI mechanism but by the CL2 mechanism. We expect that the CL2 mechanism will continue to dominate even after our experimental period ($t = 600\ T_w$) because the enstrophy budget achieved an almost steady state in the mature stage.

Our DNS was set up with the similar initial wave conditions and stratification, and the same water depth as the laboratory experiment by Dai et al. (2010) where the LI mechanism was suggested to occur. However, the analysis of the simulated field shows that the LI mechanism did not work in our DNS. Additionally, the estimated vertical eddy diffusivity was smaller than the parameterized vertical eddy diffusivity ($B\upsilon$) which explains the destratification observed in the laboratory experiment by Dai et al. (2010). These inconsistencies may result from the differences in experimental setup between the laboratory experiment and our DNS, such as domain size and boundary conditions. Larger domain size allows more active interaction between surface waves that may change interaction between orbital motion and turbulence, though the proposed LI mechanism does not explicitly assume such processes. Wall boundaries in the tank may affect the turbulence in the laboratory experiment; periodic side boundaries (no wall boundaries) in our DNS are more appropriate to simulate the nonbreaking wave-induced turbulence in the open ocean.

Regarding the real open ocean, we note that the initial stratification used in Section 3 ($N^2 = 5.5 \times 10^{-2}\ \mathrm{s}^{-2}$), which is similar to that in Dai et al. (2010), is one order of magnitude larger than that in the real open ocean. We further note that the wave simulated in Section 3 and 5 is fairly steep ($ak = 0.1$-0.3) and short (λ = 13-62 cm); such a steep and short wave under windless conditions can be expected in limited regions, such as coastal beaches. The sensitivity tests suggest that initial stratification and wave conditions does not affect the turbulent generation mechanism but affect the mixing intensity. In respect to the initial stratification, WL wave-induced mixing will be intensified in the real ocean surface mixed layer where the water stratification is mostly weak as in sensitivity experiments described in Section 5.1. In the point of wave condition, we can discuss magnitude of the mixing using the friction velocity, because the surface stress (squared friction velocity) is a key quantity in the CL2 mechanism. In the WL wave-induced mixing, the relevant friction velocity can be estimated from the VWS. In the case of a swell with wavelength of 100 m and amplitude of 1 m, the friction velocity is estimated to be $2.5\times10^{-6}\ \mathrm{m\ s}^{-1}$, which is one order smaller than in the case of the primary wave used in Section 3 ($3.5\times10^{-5}\ \mathrm{m\ s}^{-1}$). The WL-wave induced mixing thus seems to be much weaker for typical swells. However, total impact of the WL wave-induced mixing should be investigated in more detailed and extensive manners, partly because swells travel longer distance and partly because swells are frequent. The WL wave-induced mixing for such a long wave is beyond our scope and remains to be quantified in future studies.

The present result shows that the CL2 mechanism is the dominant mechanism of the WL wave-induced mixing in our experimental setup. This mixing is expected to occur in the real open ocean. To parameterize this mixing, a parameterization of the Langmuir turbulence, with the wind stress replaced by VWS, could be an effective approach. At the same time, we can say that wave-resolving simulations for the WL wave-induced mixing, as in this study, can be used to investigate turbulence due to nonbreaking surface-wave-induced mixing (including Langmuir turbulence mixing) if the surface stress is set as an additional external parameter. Such simulations will be conducted in our future studies.

Appendix A Streamwise shear flow

To compare the simulated xy-averaged streamwise velocity $\overline{u}^{xy}$ with analytical shear flow expected from virtual wave stress (VWS), one-dimensional diffusion equation $\partial u/\partial t = \nu\partial^2 u/\partial z^2$ was solved. The upper boundary condition was set to the VWS considering the viscous decay of the initial wave (λ = 30 cm, a = 1 cm), $\nu\partial u/\partial z = \tau_{VWS}(t) = 2\nu k^2\sqrt{gk}[a(t)]^2$ where $a(t) = a(0)e^{-2\nu k^2 t}$. The bottom boundary was set to free-slip, $\partial u/\partial z = 0$. The computational domain was set as $-h \le z \le 0$. The domain is discretized by 256 grid points and a time-step interval is $\Delta t = T_w/200$, the same as the three-dimensional DNS described in Section 3.

Figure 23 shows the vertical profiles of xy-averaged streamwise velocity simulated by the three-dimensional DNS with an initial perturbation ($\overline{u'_{3D}}^{xy}$, blue line in Fig. 23) and without an initial perturbation ($\overline{u_{3D}}^{xy}$, orange line), and streamwise velocity calculated by the one-dimensional diffusion equation with virtual wave stress (u_{1D}, green dashed line) at $t = 70\ T_w$. Vertical profiles of $\overline{u'_{3D}}^{xy}$ and $\overline{u_{3D}}^{xy}$ qualitatively agree with u_{1D}, though the $\overline{u'_{3D}}^{xy}$ and $\overline{u_{3D}}^{xy}$ are slightly larger than u_{1D} at each depth. This difference probably comes from differences in the upper boundary between one-dimensional calculation (fixed at $z = 0$) and three-dimensional DNS ($z = \eta$). In fact, the u_{1D} agrees well with $\overline{u'_{3D}}^{xy}$ and $\overline{u_{3D}}^{xy}$ if the upper boundary is set at $z = -0.25$ cm. Note that the vertical profile of $\overline{u_{3D}}^{xy}$ agrees better than those of $\overline{u'_{3D}}^{xy}$, which indicates that vortex pairs render the vertical distribution of streamwise velocity.

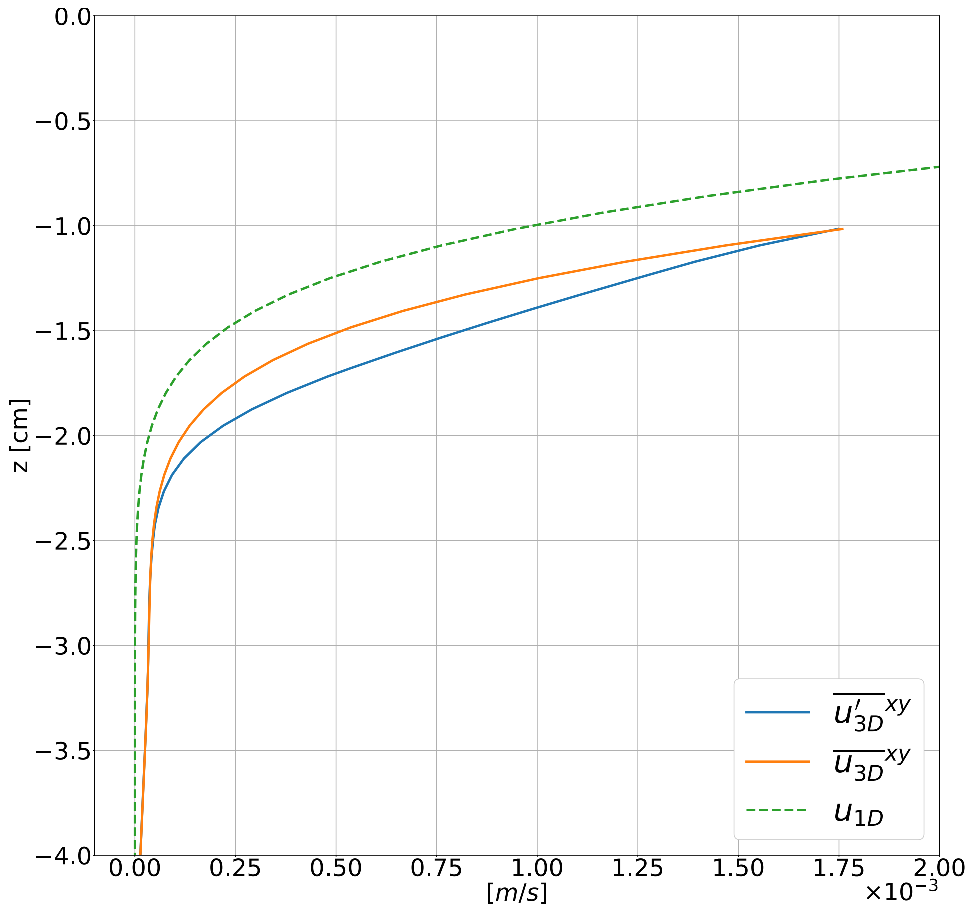

Fig. 23 Comparison of the vertical profiles of xy-averaged streamwise velocity simulated by the three-dimensional DNS with an initial perturbation ($\overline{u'_{3D}}^{xy}$) and without an initial perturbation ($\overline{u_{3D}}^{xy}$), and streamwise velocity calculated by the one-dimensional diffusion equation with virtual wave stress (u_{1D}) at $t = 70\ T_w$

Acknowledgements We thank Mr. Takeshi Yamashita at Cyberscience Center, Tohoku University, for his technical assistance with the numerical simulation. Some experiments were conducted using the supercomputer resources at Cyberscience Center, Tohoku University.

Author Contributions Conceptualization: H.I., Y.Y.; Methodology: H.I., Y.Y.; Software, Investigation, Visualization and Writing - original draft: H.I.; Writing - review and editing: Y.Y., Y.F.; Supervision: Y.Y.

Funding This research was supported by JSPS KAKENHI Grant Numbers 19H01618 and 22H00178.

Data Availability The data that support the findings of this study are available upon request.

Declarations

Ethical Approval and Consent to participate Not applicable

Human Ethics Not applicable

Consent for publication Not applicable

Competing interest The authors declare no competing interests.

References

Babanin A (2006) On a wave-induced turbulence and a wave-mixed upper ocean layer. Geophys Res Lett 33. https://doi.org/10.1029/2006GL027308

Babanin AV, Haus BK (2009) On the existence of water turbulence induced by nonbreaking surface waves. J Phys Oceanogr 39:2675–2679. https://doi.org/10.1175/2009JPO4202.1
Beyá J, Peirson W, Banner M (2012) Turbulence beneath finite amplitude water waves. Exp Fluids 52:1319–1330. https://doi.org/10.1007/s00348-011-1254-4
Bogucki DJ, Haus BK, Barzegar M et al (2020) On the nature of the turbulent energy dissipation beneath nonbreaking waves. Geophys Res Lett 47:e2020GL090138. https://doi.org/10.1029/2020GL090138
Chen S, Qiao F, Huang C et al (2018) Effects of the non-breaking surface wave-induced vertical mixing on winter mixed layer depth in subtropical regions. J Geophys Res Oceans 123:2934–2944. https://doi.org/10.1002/2017JC013038
Craik AD, Leibovich S (1976) A rational model for Langmuir circulations. J Fluid Mech 73:401–426. https://doi.org/10.1017/S0022112076001420
Dai D, Qiao F, Sulisz W et al (2010) An experiment on the nonbreaking surface-wave-induced vertical mixing. J Phys Oceanogr 40:2180–2188. https://doi.org/10.1175/2010JPO4378.1
D'Asaro EA (2014) Turbulence in the upper-ocean mixed layer. Annu Rev Mar Sci 6:101–115. https://doi.org/10.1146/annurev-marine-010213-135138
Fujiwara Y, Yoshikawa Y, Matsumura Y (2018) A wave-resolving simulation of langmuir circulations with a nonhydrostatic free-surface model: Comparison with Craik-Leibovich theory and an alternative Eulerian view of the driving mechanism. J Phys Oceanogr 48:1691–1708. https://doi.org/10.1175/JPO-D-17-0199.1
Fujiwara Y, Yoshikawa Y, Matsumura Y (2020) Wave-resolving simulations of viscous wave attenuation effects on Langmuir circulation. Ocean Model 154:101679. https://doi.org/10.1016/j.ocemod.2020.101679
Grant AL, Belcher SE (2009) Characteristics of langmuir turbulence in the ocean mixed layer. J Phys Oceanogr 39(8):1871–1887. https://doi.org/10.1175/2009JPO4119.1
Hu H, Wang J (2010) Modeling effects of tidal and wave mixing on circulation and thermohaline structures in the bering sea: Process studies. J Geophys Res Oceans 115. https://doi.org/10.1029/2008JC005175
Leibovich S (1983) The form and dynamics of langmuir circulations. Ann Rev Fluid Mech 15:391–427. https://doi.org/10.1146/annurev.fl.15.010183.002135
Li Q, Reichl BG, Fox-Kemper B et al (2019) Comparing ocean surface boundary vertical mixing schemes including langmuir turbulence. J Adv Model Earth Syst 11:3545–3592. https://doi.org/10.1029/2019MS001810
Longuet-Higgins MS (1953) Mass transport in water waves. Philos Trans R Soc Lond Ser A Math Phys Sci 245:535–581. https://doi.org/10.1098/rsta.1953.0006
Pleskachevsky A, Dobrynin M, Babanin AV et al (2011) Turbulent mixing due to surface waves indicated by remote sensing of suspended particulate matter and its implementation into coupled modeling of waves, turbulence, and circulation. J Phys Oceanogr 41:708–724. https://doi.org/10.1175/2010JPO4328.1
Qiao F, Yuan Y, Yang Y et al (2004) Wave-induced mixing in the upper ocean: Distribution and application to a global ocean circulation model. Geophys Res Lett 31. https://doi.org/10.1029/2004GL019824
Qiao F, Yuan Y, Deng J et al (2016) Wave–turbulence interaction-induced vertical mixing and its effects in ocean and climate models. Phil Trans R Soc A Math, Phys Eng Sci 374:20150201. https://doi.org/10.1098/rsta.2015.0201
Savelyev IB, Maxeiner E, Chalikov D (2012) Turbulence production by nonbreaking waves: Laboratory and numerical simulations. J Geophys Res Oceans 117. https://doi.org/10.1029/2012JC007928
Tsai Wt, Hung Lp (2007) Three-dimensional modeling of small-scale processes in the upper boundary layer bounded by a dynamic ocean surface. J Geophys Res Oceans 112. https://doi.org/10.1029/2006JC003686
Tsai Wt, Chen Sm, Lu Gh (2015) Numerical evidence of turbulence generated by nonbreaking surface waves. J Phys Oceanogr 45:174–180. https://doi.org/10.1175/JPO-D-14-0121.1
Tsai Wt, Lu Gh, Chen Jr et al (2017) On the formation of coherent vortices beneath nonbreaking free-propagating surface waves. J Phys Oceanogr 47:533–543. https://doi.org/10.1175/JPO-D-16-0242.1
Wang S, Wang Q, Shu Q et al (2019) Improving the upper-ocean temperature in an ocean climate model (fesom 1.4): Shortwave penetration versus mixing induced by nonbreaking surface waves. J Adv Model Earth Syst 11:545–557. https://doi.org/10.1029/2018MS001494
Wu L, Rutgersson A, Sahlée E (2015) Upper-ocean mixing due to surface gravity waves. J Geophys Res Oceans 120:8210–8828. https://doi.org/10.1002/2015JC011329
Yang D, Shen L (2011) Simulation of viscous flows with undulatory boundaries. Part I: Basic solve. J Comput Phys 230:5488–5509. https://doi.org/10.1016/j.jcp.2011.02.036

Publisher's Note Springer Nature remains neutral with regard to jurisdictional claims in published maps and institutional affiliations.